Analysis and fast modelling of microstructures in duplex stainless steel formed by directed energy deposition additive manufacturing

Alexander Edwards, Daniel Weisz-Patrault, Eric Charkaluk

Analysis and fast modelling of microstructures in duplex stainless steel formed by directed energy deposition additive manufacturing

Alexander Edwards[a], Daniel Weisz-Patrault[a], Éric Charkaluk[a]

[a]*École Polytechnique, Institut Polytechnique de Paris, LMS, CNRS, F-91128 Palaiseau, France*

Abstract

Superduplex stainless steels have seen increasing use in past decades in applications that require both excellent mechanical properties and corrosion resistance. The properties of duplex steels depend strongly on their thermal history, which can produce a wide range of austenite to ferrite ratios; whereas optimal properties generally require near 50-50 ferrite-austenite duplex microstructures. Additive manufacturing processes involve large thermal gradients as new material is melted on top of already printed material, and thermal history depends on process parameters. As the equilibrium phase ratio depends strongly on temperature, the result is a wide range of reported phase ratios, ranging from negligible fractions of austenite to greater than 60 %. So it is important to understand and predict how the phase ratio depends on process parameters. We assesses the microstructures in single-bead-thickness walls of SAF 2507 superduplex stainless steel printed using constant process parameters, using the laser metal powder directed energy deposition (LMPDED) additive manufacturing technique. Post-printing microstructural analysis revealed a gradient of austenite phase fraction as a function of distance from the build platform. This data reveals the relation between the thermal history and solid-solid phase transformation of ferrite to austenite during the fabrication process. The thermal history of each position in the wall was modelled by a previous fast numerical simulation (that has been improved in this contribution), and a fast diffusion controlled solid-solid phase transformations model based on semi-analytical methods has been developed. Numerical results for the phase ratios are in reasonable agreement with experimental observations. The proposed simulations strategy is sufficiently fast to enable to adjust the process parameters to achieve a targeted distribution of phase ratio in order to facilitate additive manufacturing of super duplex stainless steels, and a temperature control strategy of the build platform has been proposed on this basis to reach almost uniform near 50-50 phase ratios.

Keywords: Duplex steel, Directed Energy Deposition Additive Manufacturing, Microstructure, Phase proportions gradients

1. Introduction

Significant progress in additive manufacturing (AM) technologies, also called 3D printing, have taken place over the last decade. These technologies have the potential to revolutionise manufacturing for several reasons: minimal material waste, flexibility in the geometry and designs of

*Corresponding author: *daniel.weisz-patrault@cnrs.fr*

components, short time-to-market, and the possibility of producing functionally graded materials. However, applications are restricted by the unpredictability of the product properties, as porosity, microstructure and residual stresses, which all depend on product geometry and processing parameters. Therefore it is essential to develop realistic numerical models that can predict, and so control, these properties before the product is printed. Directed energy deposition (DED) is a form of additive manufacturing (AM) in which a heat source melts extra material layer by layer onto a substrate. In laser metal powder directed energy deposition (LMPDED), metal powder is fed coaxially with a laser. As shown in figure 1, the powder is transported by a cover gas through the nozzle to the build platform (i.e., substrate), where it is melted by the laser to form a melt pool. The nozzle moves parallel with the substrate in order to form beads of metal alloy. Each bead can act as a foundation for subsequent beads, building the final product layer by layer.

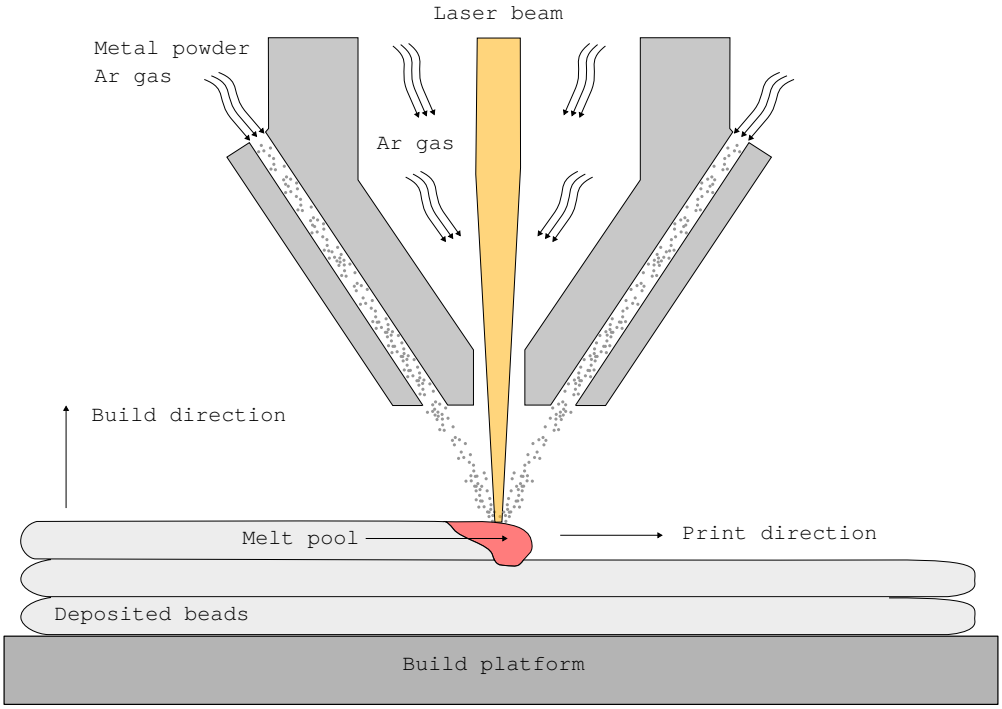

Figure 1: Schematic representation of laser metal powder directed energy deposition. This figure is inspired by Lim et al. [1]

This results in complex, time-dependent temperature profiles within the fabricated part. Each point on the product is likely to experience repeated heating and cooling cycles. This may not be a significant problem for single phase alloys, like 316 austenitic stainless steel, but precipitation-hardening alloys or duplex steels can undergo solid-solid phase transformations which vary with position and process parameters [2].

Duplex stainless steels (DSS) combine many of the beneficial properties of ferritic and austenitic steels. The excellent strength, toughness and fatigue resistance that duplex steels offer are a result of the balance between the body-centered cubic (BCC) and face-centered cubic (FCC) phases (i.e. two phase *duplex* microstructures) [3]. *Super* DSS have higher concentrations of Cr, Mo,

N which increase its resistance to pitting and crevice corrosion, indicated by a pitting resistance equivalent number (PREN) over 40 [3]. Such alloys have seen increasing use in recent decades in marine, petrochemical, and other applications which need a combination of excellent mechanical properties and corrosion resistance [4]. Compared to austenitic steels (like 316 steel), duplex steels are enriched in Cr, Mo and N, and purposefully poorer in Ni, which enables a 50-50 ratio of austenite and ferrite around 1400 K [5]. DSS are designed to solidify *ferritically* (ie. initially 100 % ferrite), which requires a mono-ferritic temperature region near the melting point [3]. Austenite precipitates by solid-solid phase transformation in the ferrite at slightly lower temperatures. Ramirez et al. [6] reported that the super SAF 2507 DSS quenched from a *ferritization* temperature of 1623 K was not completely ferritic; however, Hertzman et al. [7] had already found experimentally that in this alloy 100 % ferrite only occurs in a higher temperature range: between 1653 and 1658 K. Pettersson et al. [8] confirmed the finding that SAF 2507 shows a region of 100 % ferrite near the melting point, and concluded that equilibrium calculations generally over-estimate austenite stability (especially near the melting point). An exception is the adjustment of Thermocalc [9] by Calliari et al. [5], which correctly represents the experimental data near the melting point of SAF 2507.

However, application of AM to duplex steels has been limited by the inability to form a consistent ferrite/austenite microstructure in the as-printed material. Duplex steels are known to present a range of equilibrium austenite (i.e., γ) to ferrite (i.e., δ) phase fraction ratios as a function of temperature [5]. At high temperatures near the melting point ferrite is favoured relative to austenite. The equilibrium fraction of austenite then increases during cooling, as shown in figure 2, but the kinetics of the transition slows. As a result, the room-temperature fraction of austenite depends on the thermal history. A balanced austenite/ferrite ratio could be achieved by subsequent annealing at around 1400 K [10, 11]; however, not only is this an additional manufacturing step which can lead to dimensional changes, but in some applications, such as repair of existing components, it is impossible.

Thus to better understand and predict how the phase ratio depends on process parameters, this study assesses the microstructures and proportion of austenite to ferrite in single bead thickness walls of SAF 2507 super-duplex stainless steel printed via LMPDED. The experimental analysis is complemented by a numerical simulation of temperature fields, and solid-solid phase transformations arising during the printing process. The model was checked against the experimental data and offers a fast tool to adjust the process parameters to reach a targeted distribution of phase fraction. This is especially important for DSS because of their sensitivity to thermal history. Solid state phase transitions are considered as a post-processing of the temperature field computation. The proposed simulations strategy should fast enough to enable to adjust the process parameters to achieve a targeted distribution of phase ratio in order to facilitate additive manufacturing of super duplex stainless steels.

In the literature there are only a few papers on AM of DSS [12]: they use laser powder bed fusion (LPBF) (also referred to as selective laser melting (SLM)), wire arc additive manufacturing (WAAM), and directed energy deposition (DED) with wire or powder. The few examples of duplex steel printed by AM have shown a wide range of phase ratios in as-printed specimens: from almost fully ferritic microstructure using LPBF [10] to up to 80 % austenite microstructures for WAAM [13]. The LPBF printing process is known to have exceptionally high cooling rates (in

the range of 10^5 to 10^7 K.s^{-1}) [14]. Thus [10, 11, 14] have shown only a negligible fraction of austenite forms, located exclusively along ferrite-ferrite grain boundaries (overall less than 1 % γ). Therefore post-printing treatment was needed to reach the desired 50-50 ratio. By contrast, [13, 15] found microstructures to be predominantly austenite after WAAM. This technique builds the product by adding successive arc welding beads, so it applies orders of magnitude more energy than powder-based AM (400-870 J.mm^{-1} [13], compared to around 0.355 J.mm^{-1} in LPBF [10]). However, in WAAM, the austenite fraction reached even 73-85 %, because the cooling rates are slower as the melt-pool is not always surrounded by a massive heat-sink; and furthermore the deposited material can get reheated by subsequent passes to temperatures which favours austenite precipitation. DED uses energies intermediate between those in LPBF and WAAM. Brázda et al. [16] applied 28.3-49.5 J.mm^{-1} when printing super-DSS using LMPDED (unfortunately they did not specify their powder mass flow rate during the printing to allow more effective comparison of printing parameters). They printed microstructures with 30 to 38 % austenite, showing primary ferrite grains with a layer of grain boundary (GB) austenite. The GB layer was much thicker than that in LPBF. At higher austenite fractions, austenite also penetrated the ferrite grains in the form of Widmenstätten plates and ultimately formed globular intragranular austenite. In a more detailed description of LMPDED printing of super-DSS, Iams et al. [17] found it is possible to achieve 58.3 % austenite fraction with a higher energy rate of 188.7 J.mm^{-1}. They also reported that, within a single printed part, austenite fraction increased with distance from the substrate: from 55 % at 5-10 mm to 70 % at 20 mm. Thus they had rather too much austenite (65 %) and the phase fractions were not constant in the printed part.

Considering these difficulties, a natural idea is to simulate the AM process and phase transition so that the process parameters can be optimized in order to reach a targeted phase fraction ratio. Regarding numerical approaches to compute temperature fields in LMPDED, many papers focus on very detailed simulations at the mesoscopic scale, especially powder melting, the hydrodynamic problem, and crystallization during cooling (e.g., [18–20]). However, such numerical simulations are often limited to a single layer, and cannot capture phase gradients in the entire part. Macroscopic simulations have also been developed (e.g., [21–23]) but are still computationally costly. Thus, simplified linear thermal analyses have been proposed (e.g., [24, 25]), which neglect the latent heat of fusion, and are limited to simple flat-wall geometries. In this paper, a fast numerical approach [26, 27], which can deal with complex geometry and takes account of latent heat release during solidification, is used. This approach to temperature modelling has already been validated experimentally by infrared measurements using a pyrometer [26] and an infrared camera [28], and was used to predict residual stresses [28] and grain growth [29–31]. Some improvements have been implemented in this contribution to capture more precisely the effect of the laser power, the latent heat of fusion, and the build platform temperature evolution in order to accurately predict the kinetics of the ferrite to austenite phase transition.

In the literature, the ferrite to austenite phase transition in DSS has been modeled in different ways. For instance, Johnson-Mehl-Avrami equation has been fitted on experiments [32, 33]. However the present paper takes into account that most austenite grows from the grain boundaries. So the ferrite grain size is taken into account, and a diffusion controlled growth model is applied to estimate austenite growth from the boundaries. A well known diffusion controlled growth theory has been proposed by Bhadeshia [34], which relies on a simple analytical solution of the

diffusion equation in a 1D infinite slab. However, when the diffusion zone joins at the grain center (i.e., mechanism refereed as *soft impingement*) the infinite slab approximation is no longer valid, and the approach should be adapted. To avoid approximation issues, the usual strategy [35–37] is to numerically solve a 1D diffusion problem in a finite slab with mass conservation in the grain (i.e., no mass exchange with other grains). In addition, as for the classical theory [34], the composition of ferrite and austenite at their mutual interface is considered to be in local equilibrium. In this contribution, a similar approach is derived, but since fast computation time is aimed, semi-analytical solutions are exploited.

The paper is organized as follows. The experimental study is presented in section 2 and the microstructure and phase proportion are discussed with respect to process parameters. The improvements to the thermal analysis proposed in [26] are broached in section 3.1. The diffusion-controlled growth model is derived in section 3.2. Material properties are detailed in section 4, and the comparison of the simulations with experimental results is presented in section 5. Finally, the effect on the ferrite to austenite ratio of preheating the substrate or even control its temperature during fabrication is investigated in section 6, and conclusive remarks are given in section 7.

2. Experimental study

2.1. Materials and method

A series of SAF 2507 DSS walls were built via DED using a BeAM Mobile-004 machine equipped with a Itterbium YLR fibre laser (1070 nm wavelength) and a 500 W maximum power output. The walls were constructed using a powder feedstock of SAF 2507 DSS made by Sandvik, with a 77.6 µm average powder particle diameter and 98.4 % of particles in the range of 45-99 µm. The composition was verified by Sandvik and corresponded to the SAF 2507 DSS norms. The nominal powder composition is given in table 1.

The walls were built to single bead thickness by layering single beads on top of each other. No dwell time was applied and the printing direction alternated between layers. The printing was carried out using the DSS powder starting on a 316 austenitic stainless steel substrate. The length of the wall was set to 50 mm (X direction). The height was controlled by the increment in Z between layers (0.15 mm) and the number of layers, which was adjusted to achieve 15 mm of wall height from the substrate (100 layers). The printing speed was 2000 mm.min^{-1}, with 225 or 250 W laser power, and 7.1 g/min powder flow rate.

The printed walls were then cut along the plane perpendicular to the printing direction X to make cross section samples. These samples were then set in conducting epoxy resin and polished. Polishing was carried out using grinding paper down to P4000 (5 µm), then diamond paste polishing with 3 µm, followed by 1 µm. The final polishing step consisted of ion polishing using 6 kEV, 6 rpm and an incident angle of 6 degrees. The microstructures of the samples were analysed in a scanning electron microscope (SEM) using electron backscatter diffraction (EBSD) in a Quanta 600 with an oxford Instruments X detector which enables maximum frame rate of 3000 Hz. The results of the equilibrium calculations made using Thermocalc [9] are shown in figure 2. This equilibrium calculation serves two purposes: firstly in this experimental section it will give us a better understanding of the microstructures formed during the printing process, secondly for the

numerical simulation of the printing process and solid-solid phase transformations, it will give us the equilibrium element partitioning between ferrite and austenite at different temperatures.

Thermocalc predicts a rather large range of temperatures from 1602 to 1670 K with fully ferrite phase (and excess nitrogen). This corresponds to the fully ferritic phase regime calculated in [5], whose temperature range lies roughly between 1600 and 1650 K. Experimental evidence confirms the presence of this high temperature mono-ferritic phase [7] but over a much narrower range of temperatures (1653-1658 K). Equilibrium calculations have a tendency to overestimate austenite stability according to [8] and present no ferrite regime, fortunately this is not an issue with the equilibria here in figure 2.

Starting from 1602 K, the top of the $\delta + \gamma$ phase region, as the temperature falls the equilibrium fraction of austenite increases and eventually becomes the majority phase (the 50-50 inflexion point is near 1400 K, which is consistent with [5]). At lower temperatures, below 1330 K the fraction of sigma phase increases dramatically at the expense of the ferrite. Jacob and Povoden-Karadeniz [38] confirmed the presence of sigma phase at 1273 K and below, consistent with [5] calculation. Formation of sigma phase however is heavily time dependent as the kinetics of diffusional phase transformations is much slower than at higher temperatures.

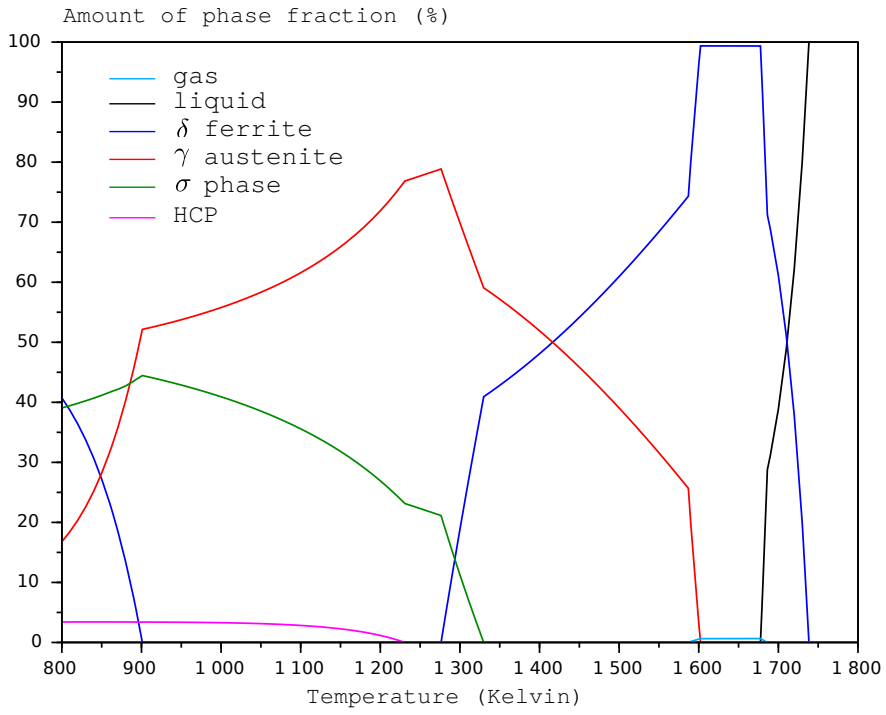

Figure 2: Diagram of phase fractions vs temperature for equilibria calculations using ThermoCalc [9].

Phase equilibria for 2507 duplex steel as a function of temperature were calculated using ThermoCalc TCFE9 database using system conditions: pressure 10^5 Pa, system size 1 mole, alloy composition according to table 1.

Table 1: Nominal DSS Alloy Composition SAF 2507 DSS in wt %

Fe	Ni	Cr	Mo	Mn	N	C	Si	P	Cu	S
Balance	7	25	4	1.2	0.285	0.03	0.8	0.035	0.5	0.02

2.2. *Experimental results*

The section taken from the as-printed duplex steel wall is illustrated in figure 3. The red highlighted area represents the surface area analysed by EBSD and presented in figures 4 and 5. Figure 4 illustrates the distribution and form of austenite (red) and ferrite (blue) phases. Super duplex steel is expected to solidify initially as 100 % ferrite, this is illustrated by the distribution of austenite mostly along prior ferrite-ferrite GBs. Subsequent austenite growth also occurs into the existing grains of the ferrite matrix as Widmenstätten plates and intragranular precipitates [16]. The ferrite only EBSD inverse pole figure map of figure 5 illustrates the morphology of the ferrite grains. The solidification of the material begins near the wall surface on the left and right hand sides, here the ferrite grains have predominantly equiaxed morphology. A few of these grains with favourable crystal orientation relative to the thermal gradient grow in towards the middle of the wall via epitaxial growth giving elongated grains. The direction of the epitaxial growth is slanted towards the middle, following the thermal gradient as heat escapes via convection at the wall surface and conduction down to the substrate.

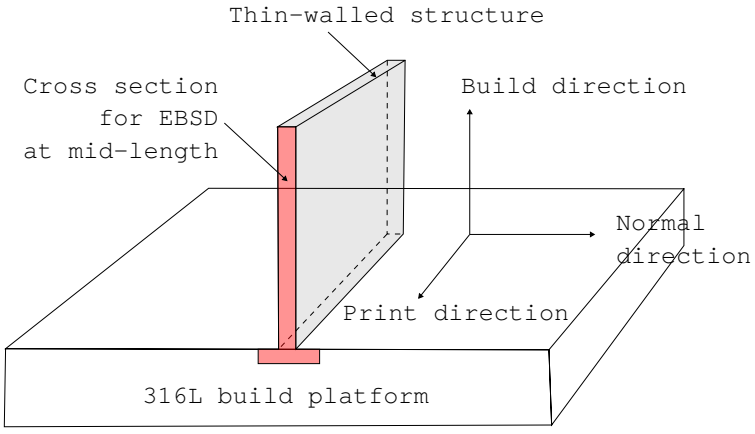

Figure 3: Illustration of the section of the wall, with the EBSD map area highlighted in red.

The texture of these ferrite grains is analysed using pole figures in figure 6 which shows that in DSS the epitaxial ferrite grain growth follows predominantly the [100] direction [39]. The EBSD map can be broken down into 5 areas from left to right. We observe that the 1-st and 5-th areas near the surface of the wall present negligible texture with equiaxed grains. In the second and fourth sections the epitaxial grains grow at an angle of approximately 35-45 degrees towards the centre following the [100] direction. Right in the middle the grain growth is no longer inclined with respect to the surface to the left or right, but rather towards the build direction (out of the page).

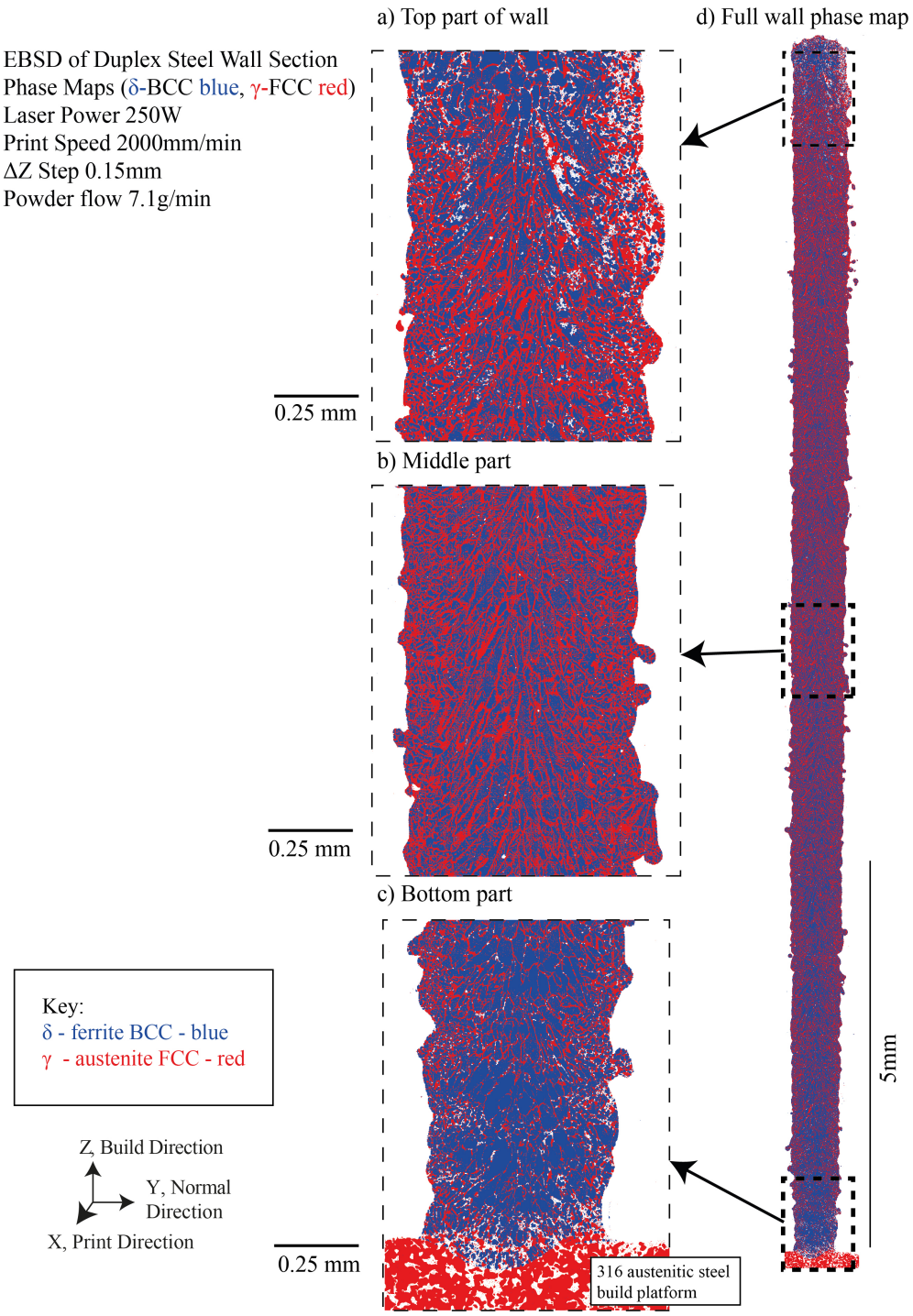

Figure 4: EBSD phase map of AM wall cross-section 250 W

The grain size of the equiaxed grains within the first 100 µm of the wall surface is of the order of 10 µm. One expects to observe relatively small grains in duplex steel because austenite formed

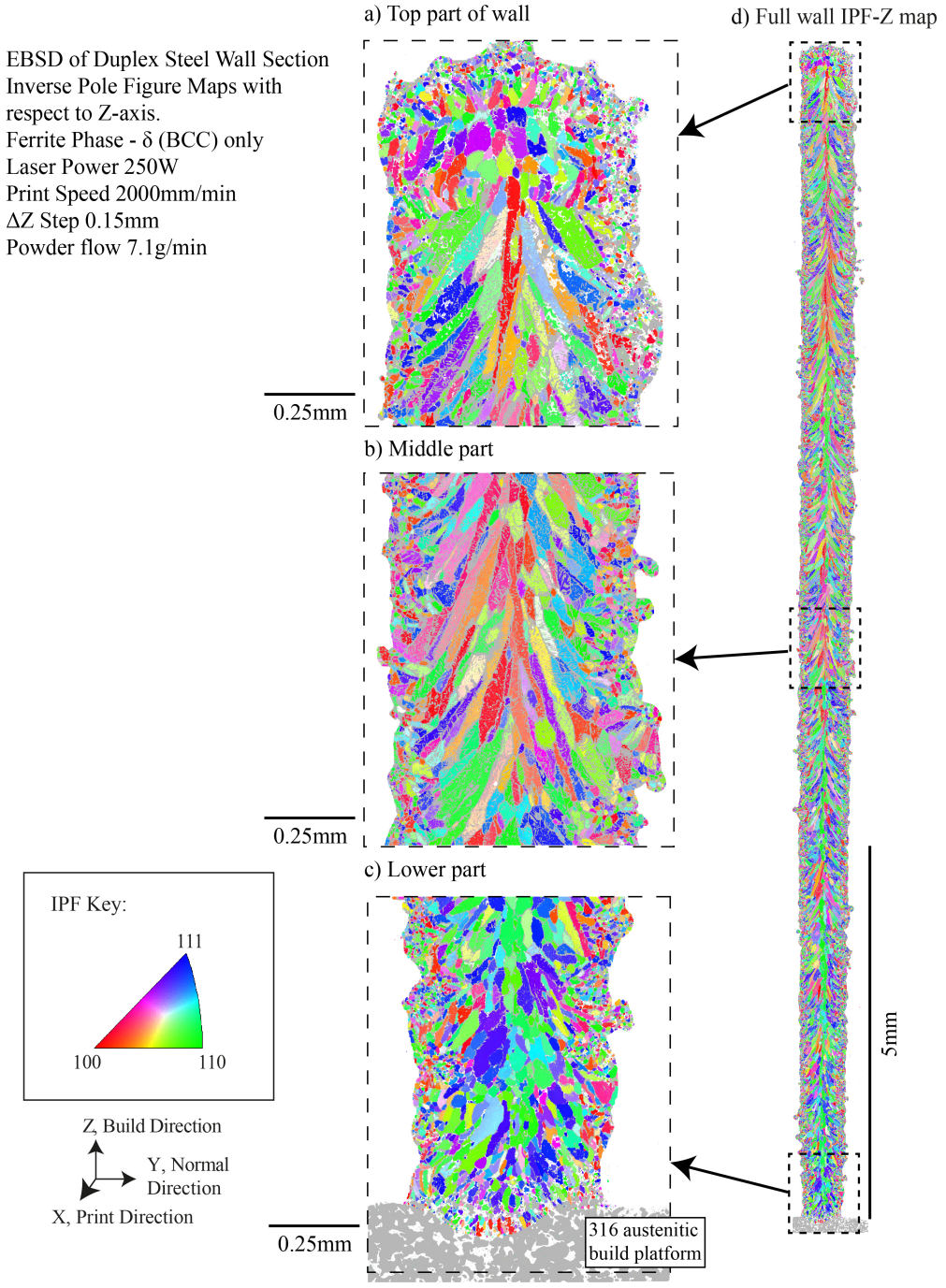

Figure 5: EBSD inverse pole figure map of the ferrite BCC phase of AM wall cross-section 250 W

at the ferrite GBs inhibits the usual coarsening of ferrite grains by ferrite-ferrite GB mobility. The longer epitaxial grains that grow in from the wall surface show a wider range of sizes: they can grow even to 100 µm in length, but are on average 50 µm long, and 20 µm wide. An accurate

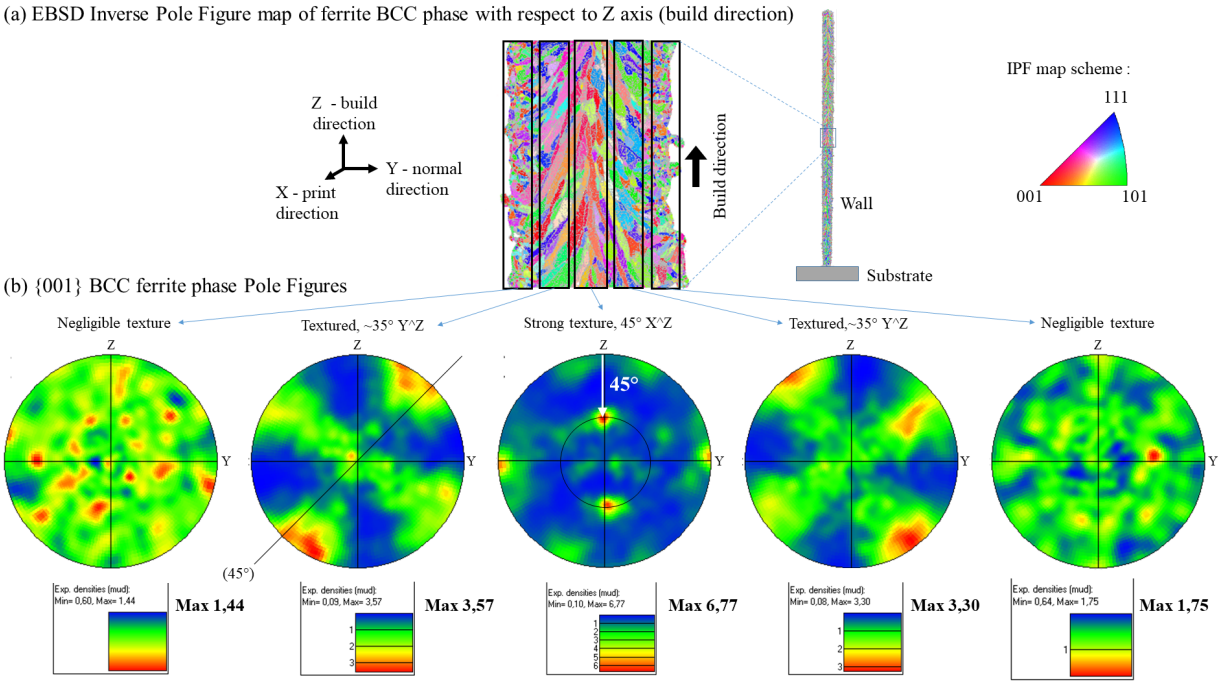

Figure 6: [100] Pole figures of ferrite phase giving the textures of AM wall as a function of depth from the wall surface, 250 W

measure of the original ferrite grain size is relatively difficult due to the presence of a high fraction of austenite. The phase map in figure 4 shows how the austenite grows in the matrix of ferrite mostly along the prior ferrite grain boundaries. This is due to the necessary partitioning of the alloying elements between the newly formed austenite and existing ferrite matrix. The diffusion of alloying elements therefore limits the growth of the austenite, and the relatively small grain sizes mean GBs dominate as preferential sites for austenite nucleation and growth. For the small equiaxed ferrite grains near the surface, the austenite forms exclusively along the grain boundaries. For larger epitaxial grains, where less grain boundary area is available, the austenite grows also partly into the grains as parallel dendrites[1]. These vary in their spacing, but are generally of the order of 10 µm.

As we established in the introduction, one of the most complex factors of DSS is control of the two-phase austenite-ferrite microstructure. For forged duplex steels the standard solution treatments are applied at temperatures near 1100 °C where the ratio of austenite to ferrite is close to 50-50. The following section will consider the significant effect of the complex thermal history DED has on duplex microstructure. An analysis of austenite phase fraction as a function of distance from the substrate was made in figure 7 by extracting row by row the data from the phase map

[1]In literature these are generally considered as Widmenstätten growth, however as characterised by Ohmori they should not be confused with displacively formed Widmenstätten plates. In duplex steel they are still controlled by a diffusional mechanism of element partitioning.

in figure 4. On this scatter plot, in the initial stages of printing, heat can escape quickly through the proximity of the relatively large substrate. This means cooling rates are faster, and less time is spent at high temperatures, limiting austenite growth in these initial duplex steel layers. As the printing progresses, and the layers are printed further from the substrate, the fraction of austenite increases (relatively more *red* phase is visible in figure 4). Finally, the last few layers at the end of the printing process contain less austenite (dip in the curve). There is a lack of subsequent layers reheating the structure, meaning less austenite formed.

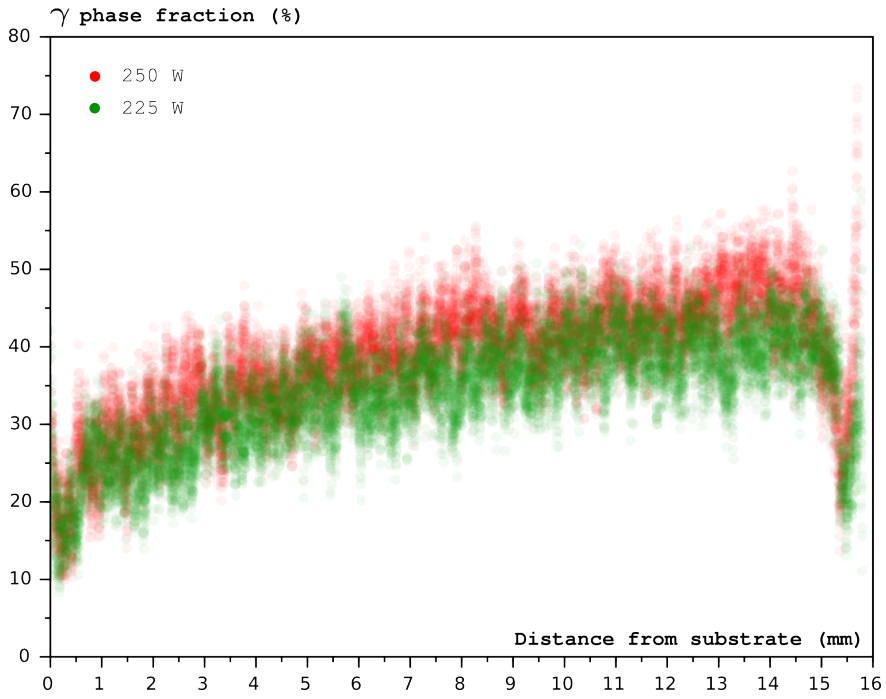

Figure 7: Graph of austenite phase fraction of the duplex printed wall as a function of distance from the substrate

3. Modeling strategy

3.1. Temperature field computation

The computation of the temperature field relies on the assumption that for single bead structures, heat fluxes along the print direction are negligible with respect to the build and normal directions. Based on this assumption a numerical strategy has been established in [26] based on analytical solutions of successive 2D multilayer composites heat conduction problems. Three improvements are proposed in this contribution to better capture the $\delta \rightarrow \gamma$ phase transition. First, the deposition temperature denoted by T_{dep} is a parameter corresponding to the melt pool temperature, and has been calibrated for specific process parameters. In this contribution, since two experiments have been performed with two different laser power, the deposition temperature is approximated as in

[28] by the following analytical form [40]:

$$T_{\text{dep}} = \frac{IR_{\text{beam}}}{\sqrt{\pi}\lambda_{\text{liq}}} \arctan\left(2\frac{\sqrt{D_{\text{liq}}t_{\text{beam}}}}{R_{\text{beam}}}\right) \tag{1}$$

Where R_{beam} is the laser beam radius, λ_{liq} and D_{liq} are respectively the thermal conductivity and diffusivity of the liquid metal, $I = P_{\text{beam}}/(2\pi R_{\text{beam}}^2)$ and $t_{\text{beam}} = R_{\text{beam}}/V_{\text{beam}}$ with V_{beam} the laser beam velocity.

The second improvement is related to the latent heat of fusion. Indeed, the latent heat of fusion was taken into account in [26] by interpolating the liquid to solid phase transition rate on a series of time decreasing exponential functions. However, the heat source due to the phase transition does not start immediately after the deposition of the molten metal, but only when the temperature reaches the liquidus temperature T_{liq}. This delay being difficult to capture with time decreasing exponential functions, the heat source was applied at $t = 0$ directly when the molten metal is deposited. If this approximation is acceptable to capture the temperature kinetics of the solid material, the cooling rate during solidification cannot be estimated accurately. As detailed in the following, the studied $\delta \rightarrow \gamma$ phase transition depends on the grain size of the solidified δ phase, which highly depends on the cooling rate during solidification. Therefore, the approach proposed in [26] has been improved to correctly address the cooling rates during solidification. To do so, a new initial condition is set at $t = t_{\text{liq}}$ when $T = T_{\text{liq}}$ (where t denotes the time and T the computed temperature), and the heat source due liquid to solid phase transition is applied.

The third improvement is related to the build platform temperature, which has a significant impact on the temperature kinetics. The substrate was assumed to be constant and homogeneous during the fabrication of each layer, which is acceptable after a certain number of layers when the laser is sufficiently far from the substrate, but rather inaccurate for the first layers. To better capture the non-uniform distribution of phase fraction along the build direction, a better estimation of the substrate temperature is proposed in this paper by solving the following non-uniform 1D heat conduction problem:

$$\frac{\partial T_{\text{sub}}^n}{\partial t}(Z,t) - D_{\text{sub}}\frac{\partial T_{\text{sub}}^n}{\partial Z^2}(Z,t) = 0 \tag{2}$$

Where T_{sub}^n is the substrate temperature during deposition of the n-th layer, t the time, Z the spatial coordinate along the print direction, and D_{sub} ($\text{m}^2.\text{s}^{-1}$) the substrate thermal diffusivity. Boundary conditions read as convection conditions:

$$\begin{cases} -\lambda_{\text{sub}}\dfrac{\partial T_{\text{sub}}^n}{\partial Z}\left(\dfrac{h_{\text{sub}}}{2},t\right) = H_{\text{build}}\left(T_{\text{sub}}^n\left(\dfrac{h_{\text{sub}}}{2},t\right) - T_{\text{build}}^n\right) \\ \lambda_{\text{sub}}\dfrac{\partial T_{\text{sub}}^n}{\partial Z}\left(-\dfrac{h_{\text{sub}}}{2},t\right) = H_{\text{plate}}\left(T_{\text{sub}}^n\left(-\dfrac{h_{\text{sub}}}{2},t\right) - T_{\text{plate}}\right) \end{cases} \tag{3}$$

where λ_{sub} ($\text{W.m}^{-1}.\text{K}^{-1}$) is the thermal conductivity of the substrate, h_{sub} its thickness, T_{build}^n is the average temperature of the bottom first layer of the part during during the deposition of the n-th layer, T_{plate} is the temperature of the plate beneath the substrate, and H_{build} and H_{plate} ($\text{W.m}^{-2}.\text{K}^{-1}$) are the heat transfer coefficients respectively between the part and the top surface of the substrate,

and between the bottom surface of the substrate and the plate underneath. In addition the initial condition reads:

$$T_{\text{sub}}(Z, t = 0) = T_{\text{sub}}^{n-1}(Z, t^{n-1}) \tag{4}$$

where $T_{\text{sub}}^{n-1}(Z, t^{n-1})$ is the temperature of the substrate at the end of the previous layer deposition. The diffusion equation (2) with boundary conditions (3) and initial condition (4) is solved analytically in Appendix A.

3.2. Diffusion controlled growth of austenite

The $\delta \rightarrow \gamma$ phase transition is controlled by diffusion of alloying elements, and arises by thickening of a continuous austenite layer formed at the ferrite GBs in a net structure. Indeed, as already mentioned for the studied alloy (i.e., SAF 2507 DSS), the primary solidification is fully ferritic. In addition, equilibrium compositions at different temperatures have been computed with ThermoCalc, and the normalized mass of N is presented at equilibrium in figure 8. Four different regimes are clearly identified and correspond to four different mechanisms. 1) During solidification (i.e., 1738-1677 K), N atoms (i.e., austenite stabilizer) are concentrating in the liquid phase. 2) At the end of solidification (i.e., 1677-1602K), since BCC is saturated in N, more than half of the total mass of N remains outside the ferrite bulk, in gas form according to ThermoCalc, which results in significant driving force to transform ferrite into austenite. 3) Thus, within a short temperature range (i.e., 1602-1587 K) all the N content outside the ferrite bulk is rapidly diffused to the forming austenite. Therefore, even though the primary microstructure is fully ferritic, a significant amount of austenite is produced assisted by fast diffusion of N. Of course, this amount is limited by the cooling rates and diffusion properties of N between 1602 and 1587 K, so that very low γ phase fraction is reported in very fast cooling processes such as LPBF, although more significant amounts are usually reported in DED with lower cooling rates. 4) When temperature decreases below 1587 K the equilibrium δ and γ mass fractions are more stable with respect to temperature. At this point, an other diffusive mechanism takes place. Indeed, Cr (i.e., ferrite stabilizer) diffuses from austenite to ferrite, and Ni (i.e., austenite stabilizer) from ferrite to austenite, which limits the phase transition rate, because both Cr and Ni are substitutionally-diffusing elements, which diffuse orders of magnitude slower than interstitial elements such as N. Both Cr and Ni could have been taken into account together in the diffusion problem below 1587 K, but only Ni has been considered as Ni and Cr share similar diffusive properties.

The phase transition is therefore computed by solving a two-species diffusion problem. First the phase transition is controlled by the fast diffusion of N between 1602-1587 K, and then the phase transition is controlled by slower diffusion of Ni for lower temperatures. However, it should be noted that the diffusion of both N and Ni should be computed simultaneously so that the Ni concentration profile is estimated at 1587 K when Ni diffusion starts to control the phase transition. Since there is a large number of different layers subjected to thermal cycling, short computation time can only be obtained by developing a numerical strategy relying on analytical solutions of the diffusion equation. The proposed approach consists in solving the same diffusion problem as in [35–37] (i.e., mass balance in the grain and equilibrium at the δ/γ interface) in a 1D finite domain (i.e., sphere, cylinder or slab). However, the diffusion equation is highly non-linear due to the mobile δ/γ interface, and temperature dependant diffusivity and equilibrium phase fractions. To

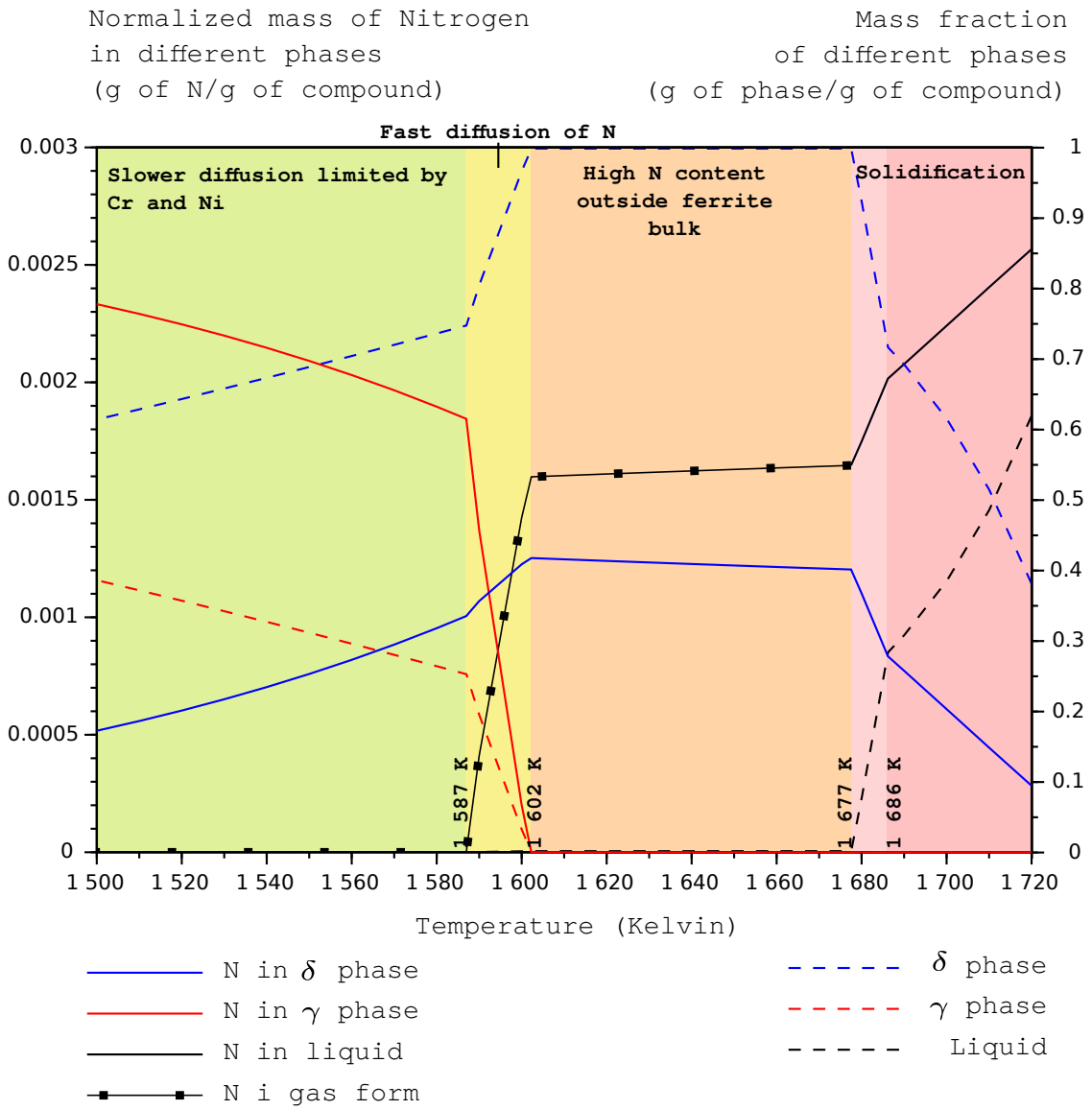

Figure 8: Normalized mass of N at equilibrium (left scale) computed as the mass of N in different phases divided by the total mass of the compound, and equilibrium mass fraction (right scale) computed as the mass of different phase divided by the total mass of the compound.

overcome this difficulty, a general analytical solution is derived for fixed δ/γ interface at constant temperature. Therefore, to correctly follow the phase transition evolution, a time discretization is introduced and the analytical solution is successively applied only during short time increments, which is consistent with the proposed assumptions (i.e., fixed δ/γ interface at constant temperature). In addition to temperature, the δ/γ interface is updated at the end of each time step based on the mass balance equation. Moreover, at each time step, a new initial condition is prescribed based on the solution concentration profile at the end of the previous time step. Of course, since between

two successive time steps the δ/γ interface is updated, the solution concentration profile is adapted to define the new initial condition in order 1) to be consistent with the new interface position and 2) to ensure that the total mass of the alloying element is unchanged.

The temperature dependant equilibrium concentrations of the alloying element in the δ and γ phases are respectively denoted by $c^{\delta}_{\text{eq}}(T)$ and $c^{\gamma}_{\text{eq}}(T)$ (where T (K) is the time dependent temperature). Moreover $w(t)$ (m) is the time dependant austenite thickness. The proposed strategy involves solving the following problem at each time step (indexed by k). The second Fick's law reads for 1D domains, $\forall t \in [t_k, t_{k+1}]$ (where t_k is the time at the beginning of the k-th time step and $t_{k+1} = t_k + \Delta t_k$ where Δt_k is the time increment):

$$\begin{cases} \dfrac{\partial c^{\delta}_k}{\partial t}(x,t) - \dfrac{D^{\delta}_k}{x^q}\dfrac{\partial}{\partial x}\left(x^q \dfrac{\partial c^{\delta}_k}{\partial x}(x,t)\right) = 0 & \text{if} \quad 0 \leq x \leq R - w_k \\ \dfrac{\partial c^{\gamma}_k}{\partial t}(x,t) - \dfrac{D^{\gamma}_k}{x^q}\dfrac{\partial}{\partial x}\left(x^q \dfrac{\partial c^{\gamma}_k}{\partial x}_{k}(x,t)\right) = 0 & \text{if} \quad R - w_k \leq x \leq R \end{cases} \tag{5}$$

where for the time step k, $c^{\delta}_k(x,t)$ and $c^{\gamma}_k(x,t)$ are the concentration profiles of the considered alloying element (i.e., N and Ni) in the δ and γ phases respectively, D^{δ}_k and D^{γ}_k ($\text{m}^2.\text{s}^{-1}$) denote the diffusivity in the δ and γ phases respectively, $w_k = w(t_k)$ (m) is the austenite thickness, x denotes the spatial coordinate, and $q = 0, 1, 2$ for slab, cylinder and sphere respectively.

Boundary conditions read, $\forall t \in [t_k, t_{k+1}]$:

$$(a) \begin{cases} \dfrac{\partial c^{\delta}_k}{\partial x}(x = 0, t) = 0 \\ \dfrac{\partial c^{\gamma}_k}{\partial x}(x = R, t) = 0 \end{cases} \qquad (b) \begin{cases} c^{\delta}_k(x = R - w_k, t) = c^{\delta}_{\text{eq},k} \\ c^{\gamma}_k(x = R - w_k, t) = c^{\gamma}_{\text{eq},k} \end{cases} \tag{6}$$

It should be noted that w_k, D^{δ}_k, D^{γ}_k, $c^{\delta}_{\text{eq},k}$, and $c^{\gamma}_{\text{eq},k}$ are assumed to be constant in $[t_k, t_{k+1}]$, and are only updated at the end of the time step. Equation (6) (a) corresponds to mass conservation in the grain (i.e., no mass transfer outside the grain), and (6) (b) corresponds to the equilibrium of the δ/γ interface.

The initial concentration profiles in the δ and γ phases are respectively denoted by $c^{\delta}_{\text{ini},k}(x)$ and $c^{\gamma}_{\text{ini},k}(x)$, hence:

$$\begin{cases} c^{\delta}_k(x, t = t_k) = c^{\delta}_{\text{ini},k}(x) & \text{if} \quad 0 \leq x \leq R - w_k \\ c^{\gamma}_k(x, t = t_k) = c^{\gamma}_{\text{ini},k}(x) & \text{if} \quad R - w_k \leq x \leq R \end{cases} \tag{7}$$

At the beginning of diffusion (i.e., for the *first time step* $k = 1$ at $T = 1602$ K), the initial concentration profile of N is assumed to be uniform and equal to the bulk concentration in the δ phase, i.e., $c^{\delta}_{\text{ini},1}(x) = 0.29$ wt % according to table 1. In addition, a nucleation thickness of the γ layer is postulated and denoted by w^{γ}_{ini}, hence $w_1 = w^{\gamma}_{\text{ini}}$. The dimensionless normalized mass of N outside the ferrite bulk at 1602 K denoted by $m^{\gamma}_{\text{eq},N} = 1.598 \times 10^{-3}$ (g of N per g of compound) (see figure 8) is entirely affected to the nucleated layer of austenite, which reads $c^{\gamma}_{\text{ini},1}(x) = m^{\gamma}_{\text{eq},N}\, R/w^{\gamma}_{\text{ini}}$, where R is the average equivalent grain radius. Furthermore, since Ni diffuses much slower, we assume that the initial concentration profile of Ni is uniform and equal to the bulk concentration in both the δ and γ phases, i.e., $c^{\delta}_{\text{ini},1}(x) = c^{\delta}_{\text{ini},1}(x) = 7$ wt % according to table 1.

For following time steps (i.e., $k \geq 2$) the initial concentration profile is based on the concentration at the end of the previous time step, which reads:

$$\begin{cases} c^{\delta}_{\text{ini},k}(x) = \dfrac{c^{\delta}_{k-1}\left(\Lambda^{\delta}_{k}\, x, t = t_k\right)}{\Lambda^{\delta}_{k}} & \text{if} \quad 0 \leq x \leq R - w_k \\ c^{\gamma}_{\text{ini},k}(x) = \dfrac{c^{\gamma}_{k-1}\left(\Lambda^{\gamma}_{k}\, x + \Gamma^{\gamma}_{k}, t = t_k\right)}{\Lambda^{\gamma}_{k}} & \text{if} \quad R - w_k \leq x \leq R \end{cases} \tag{8}$$

where:

$$\begin{cases} \Lambda^{\delta}_{k} = \dfrac{R - w_{k-1}}{R - w_k} \\ \Lambda^{\gamma}_{k} = \dfrac{w_{k-1}}{w_k} \qquad \text{and} \quad \Gamma^{\gamma}_{k} = R\left(\dfrac{w_k - w_{k-1}}{w_k}\right) \end{cases} \tag{9}$$

Where coefficients Λ^{δ}_{k}, Λ^{γ}_{k} and Γ^{γ}_{k} have been introduced to accommodate the update of the austenite thickness $w_{k-1} \rightarrow w_k$, and to ensure that the total mass of the alloying element in the grain is conserved. The analytical solution of (5) with boundary conditions (6) and initial condition (7) is derived in details in Appendix B. Even though grains or sub-structures from which austenite is forming are close to spheres or cylinders, the analytical solution has been found to be much faster for slabs. Thus, the solution for slabs has been used in practise and the slab size has been adjusted to correspond to an equivalent sphere as detailed in Appendix B.

The update of the austenite thickness is obtained from mass balance, which reads:

$$\dot{w}(t) = D^{\delta}(T(t))\frac{\partial c^{\delta}}{\partial x}(R - w(t), t) - D^{\gamma}(T(t))\frac{\partial c^{\gamma}}{\partial x}(R - w(t), t) \tag{10}$$

Thus, the update is approximated as follows:

$$w_k = w_{k-1} + D^{\delta}_{k-1}\int_{t_{k-1}}^{t_k} \frac{\partial c^{\delta}_{k-1}}{\partial x}(R - w_{k-1}, t)\mathrm{d}t - D^{\gamma}_{k-1}\int_{t_{k-1}}^{t_k} \frac{\partial c^{\gamma}_{k-1}}{\partial x}(R - w_{k-1}, t)\mathrm{d}t \tag{11}$$

Where integrals are calculated analytically as detailed in Appendix B.

4. Process parameters and material coefficients

Two experiments have been performed and the corresponding process parameters are listed in table 2. Heat transfer coefficients (HTC) have been estimated in [26] by comparing numerical results and infrared pyrometer measurements. However, the HTC between the build platform and the machine plate underneath has been decreased as the build platform was not clamped to the machine plate therefore decreasing the heat transfer coefficient.

The grain size after solidification should also be estimated because the grain equivalent radius R is directly involved in the proposed diffusion model detailed in section 3.2. Higher cooling rates are associated with lower austenite content as shorter time is spent in the temperature range where the $\delta \rightarrow \gamma$ phase transition occurs, but higher cooling rates are also associated with finer grain structure, which in turn promotes higher phase transition rate. Therefore, we consider the grain

Table 2: Simulation parameters

Number of layers	N_{lay}	(-)	100
Substrate thickness	h_{sub}	(mm)	5
Initial substrate temperature	T^0_{sub}	(K)	300
Length of wall	L	(mm)	50
Powder flow	Q	(g.min^{-1})	7.1
Layer height	h_z	(µm)	160
Layer thickness	h_y	(µm)	650
Laser beam radius	R_{beam}	(µm)	338
Laser beam speed	V_{beam}	(mm.min^{-1})	2000
Dwell time	t_{dwell}	(s)	0
Laser beam power	P_{beam}	(W)	250 (resp. 225)
Deposition temperature, see. (1)	T_{dep}	(K)	2511 (resp. 2260)
HTC part/air	H_{air}	(W.m^{-2}.K^{-1})	15
HTC part/build platform	H_{build}	(W.m^{-2}.K^{-1})	20000
HTC build platform/machine plate	H_{plate}	(W.m^{-2}.K^{-1})	500

size as a function of the cooling rate (instead of using a single measured value for all the layers) to take into account these opposite effects on phase transition kinetics for heterogeneous cooling rates along the height of the structure. In the literature, various approaches have been proposed to predict grain size, and some of them have been applied to additive manufacturing conditions [41]. A common approach proposed in [42] is to consider 1) nucleation of dendritic equiaxed grains from preexisting impurities or voluntarily added particles in the melt, 2) grain growth according to a simple analytic formula of the dendritic tip velocity [43], and 3) impingement using an Avrami equation (i.e., the proportion of grains stopping to grow due to the proximity of an other grain). However, this approach necessitates to postulate a size distribution of impurities in the melt, and has mainly been developed and used for aluminum alloys, which makes difficult to find data for duplex steels. Within the framework of fast simulation developed in this contribution a simpler empirical approach [44] enables us to relate the grain size and the cooling rate during solidification in the form of a power law:

$$R = R_0 \left(\frac{\chi}{\dot{T}_{\text{sol}}} \right)^n \tag{12}$$

Where χ and n are calibration coefficients, and $\dot{T}_{\text{sol}}$ is the average cooling rate during solidification. This empirical formula has been calibrated within the context of additive manufacturing of a Ni superalloy in [45], and for ferritic solidification in [46] for cooling rates ranging from 50 to 10^4 K.s^{-1}. Since for the 2507 duplex steel, the primary solidification is fully ferritic, the estimate reported in [46] (i.e., R_0=1 µm, $\chi = 3.2 \times 10^6$ K.s^{-1} and $n = 0.4$) has been used as a basis for the present study. From the EBSD map in figure 4, the average grain radius is roughly estimated to around 9 µm so that the estimate is slightly modified to $\chi = 2.6 \times 10^6$ K.s^{-1}. As already mentioned, the cooling rate during solidification $\dot{T}_{\text{sol}}$ is computed for each layer by using the thermal analysis proposed in [26] modified in this paper to better take into account the latent heat associated with

solidification.

In addition, thermal properties of 2507 DSS (i.e., thermal conductivity and thermal diffusivity) can be estimated as a function of temperature using softwares such as JMatPro [47] or from experimental data as reported in [48]. In this study, thermal properties are estimated for the solid phase from [48]. However, to the best of our knowledge there is no measurement of thermal properties of liquid 2507 DSS. These properties are needed in (1) to estimate the deposition temperature, which is expected to be higher than for 316L stainless steel used in [26, 28] as the liquidus is higher. Thermal conductivity and diffusivity of the liquid phase are chosen as twice the values of the solid state. The resulting value for the thermal diffusivity of the liquid may seem high for a steel (i.e., 13×10^{-6} m^2.s^{-1}), but it is consistent with very low specific heat measured at high temperature in [48].

Furthermore, diffusivity coefficients of alloying elements are classically given in the form of Arrhenius laws:

$$D = D_0 \exp\left(-\frac{Q}{\mathrm{R}\,T}\right) \tag{13}$$

where R (J.mol^{-1}.K^{-1}) is the gas constant, D_0 (m^2.s^{-1}) the pre-factor and Q (J.mol^{-1}) the activation energy. Pre-exponential factors and activation energies are extracted from the literature. Diffusion properties of N in the δ and γ phase of a DSS have been measured between 350 to 500 °C in [49] and at 1200 °C in [50]. A fit of (13) on the data provided in [49, 50] gives $D_0 = 2 \times 10^{-6}$ m^2.s^{-1} and $Q = 117000$ J.mol^{-1}, and are assumed to be identical in both δ and γ phases as observed in [49]. Furthermore, diffusion properties of Ni have been collected and analysed in [51] for various Cr-Fe-Ni alloys. A parametric formula, which depends on the metal composition, has been proposed in the spirit of the Calphad approach [52] and fitted on the experimental data. Using the fitted formula in [51] and chemical composition in table 1 one obtains for Ni diffusion parameters: $D_0 = 420 \times 10^{-6}$ m^2.s^{-1} and $Q = 218000$ J.mol^{-1} assumed to be identical for both δ and γ phases. All material properties used in the proposed simulation are listed in table 3.

As already mentioned a ThermoCalc computation has been performed to quantify the equilibrium concentrations of the different alloying elements involved in the diffusion problem, which are presented in figure 9.

5. Results analysis

In this section, the proposed thermal analysis and phase transition model are applied and compared to the tested experimental conditions. The temperature history can be extracted at any location in each layer. In this study to avoid to deal with large amounts of data, only the middle of each layer is considered at the location where the samples have been extracted. The temperature kinetics of the 1-st layer is presented in figure 10 for both tested conditions. Temperature cycles clearly show that the temperature range where the $\delta \rightarrow \gamma$ phase transition occur is reached several times. Diffusion profiles of Ni are presented in figure 11 for the first layer at different times in order to understand the diffusion mechanisms. The initial γ layer is fixed to 5 % of the total cell size R in order to avoid extremely thin time discretization if nearly zero thickness were chosen. (Several computations with different initial thicknesses show that 5 % leads to similar results with much coarser time discretization than smaller initial austenite thicknesses). As already mentioned, the

Table 3: Material parameters

Liquidus temperature	T_{liq}	(K)	1738
Solidus temperature	T_{sol}	(K)	1677
Thermal conductivity of the liquid metal	λ_{liq}	(W.m^{-1}.K^{-1})	30
Thermal diffusivity of the liquid metal	D_{liq}	(m^2.s^{-1})	13×10^{-6}
Thermal conductivity of the solid metal	λ_{sol}	(W.m^{-1}.K^{-1})	15
Thermal diffusivity of the solid metal	D_{sol}	(m^2.s^{-1})	6.5×10^{-6}
Density	ρ	(kg.m^{-3})	7830
Latent heat of fusion	L_f	(J.g^{-1})	300
Pre-exponential factor for N in (13)	D_0	(m^2.s^{-1})	2×10^{-6}
Activation energy for N in (13)	Q	(J.mol^{-1})	11700
Pre-exponential factor for Ni in (13)	D_0	(m^2.s^{-1})	420×10^{-6}
Activation energy for Ni in (13)	Q	(J.mol^{-1})	21800
Reference grain size in (12)	R_0	(µm)	1
Reference cooling rate in (12)	χ	(K.s^{-1})	2.6×10^6
Exponent in (12)	n	(-)	0.4

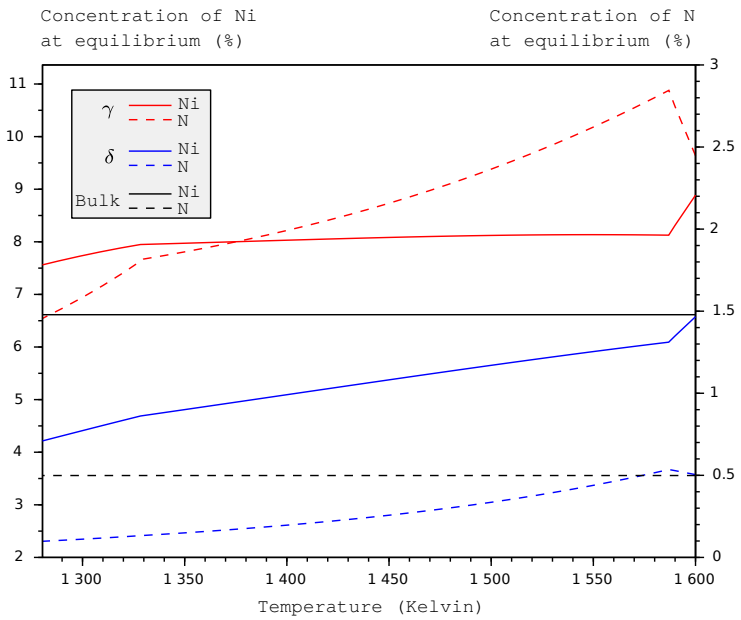

Figure 9: Equilibrium concentration of Ni and N in mol %.

initial Ni concentration is uniform and equal to the bulk concentration 6.61 mol % (i.e., 7 wt %) as listed in table 1. When the phase transition is assisted by N diffusion (i.e., red dot lines in figure 11), Ni atoms diffuse from ferrite to austenite as the equilibrium concentration in the γ side c_{eq}^{γ} is larger than the initial bulk concentration. As a result, when the phase transition starts to be

limited by Ni diffusion (i.e., red solid lines in figure 11), the Ni concentration in the austenite layer is around 8 to 8.5 mol %, although the equilibrium concentration c_{eq}^{γ} decreases. This results in an additional driving force to move the δ/γ interface in the direction of austenite thickening, as detailed in (10). In the δ side, when the phase transition is assisted either by N diffusion or by Ni diffusion (i.e., blue dot and solid lines in figure 11), the equilibrium concentration of Ni c_{eq}^{δ} is lower than the initial bulk concentration, resulting in a driving force to move the δ/γ interface in the direction of the austenite thickening.

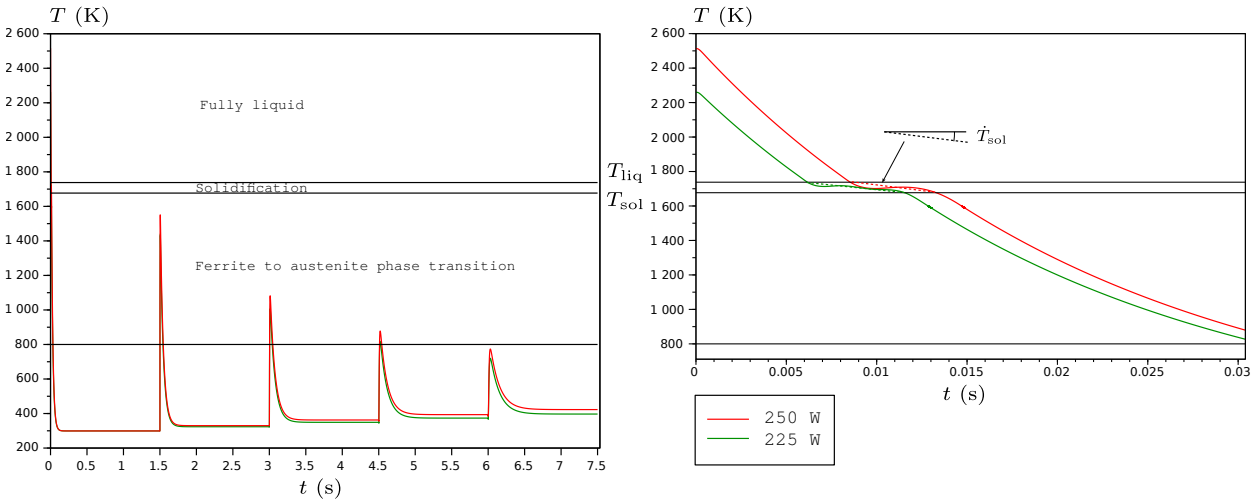

Figure 10: Computed temperature cycles (left) and magnification (right) (1st layer, 250 W and 225 W).

A comparison between measured and computed γ phase fraction is presented in figure 12 as a function of the position with respect to the build platform, where raw data presented in figure 7 have been averaged to obtained a single value by layer as for the computation. A reasonable agreement is observed for both the experiments corresponding to different laser powers (i.e., 225 and 250 W). Lower power results in lower melt pool temperature and higher cooling rates, which tend to reduce the amount of the product γ phase. However, this effect is mitigated by the fact that higher cooling rates leads to finer grain structure, which promote faster phase transition. This explains the fact that the difference between the measured phase fractions of both experiments is relatively small.

Heterogeneous phase fraction profiles are obtained according to the history of the temperature field. The first layers cool down faster because of the influence of the build platform acting as heat sink and resulting in lower γ phase fractions. Cooling rates decrease with the distance to the build platform because the melt pool is further and further from the heat sink whose temperature increases with time. This structural effect tends to a nearly steady state after more than half of the total number of layers in the tested conditions.

Furthermore, the last few layers undergo less thermal cycling than previous layers due to the interruption of fabrication, which results in a significant decrease of the transformed phase fraction. Indeed, thermal cycling plays a significant role as shown in figure 13.

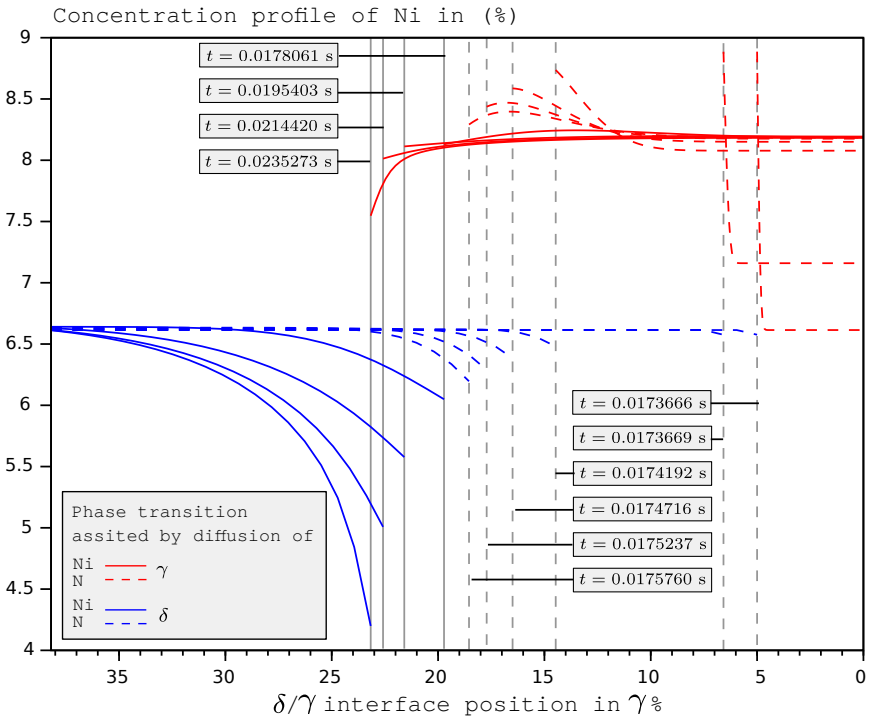

Figure 11: δ/γ interface and Ni concentration profile in mol % at different times when phase transition is assisted by N and Ni diffusion respectively (1st layer, 250 W).

6. Numerical investigation for controlling phase distribution

In section 5 the influence of laser power, other things being equal, has been demonstrated. In this section, the effect of controlling the substrate temperature on the phase transition distribution is numerically investigated in order to reach a more uniform and balanced δ/γ phase ratio. Excepted for the tested parameter all process parameters are identical to those listed in table 2 (with laser power P_{beam} set to 250 W).

First the effect of preheating the build platform is investigated. That is to say that the initial temperature of the build platform is prescribed, and then when the fabrication starts, the heating device is shut down so that the build platform temperature naturally evolves with the laser input. Three different initial build platform temperatures have been tested (300 K, which the reference computation without preheating, 600 K and 800 K). Resulting γ phase fraction profiles are presented in figure 14. It is clear that pre-heating enables to reach higher austenite phase fraction for the first half of the part. Indeed, as a result of the build platform preheating lower cooling rates take in the temperature range where N and Ni can diffuse leading to higher austenite phase fraction. However, when the number of layers increases the local temperature around the melt pool becomes more independent from the build platform temperature and therefore the austenite phase fraction tends to stabilize near the reference computation. The main effect of a significant preheating of the build platform is only to obtain slightly more uniform phase fraction distribution but without significantly modifying the target δ/γ ratio in the stabilized region. To reach even more uniform phase fraction

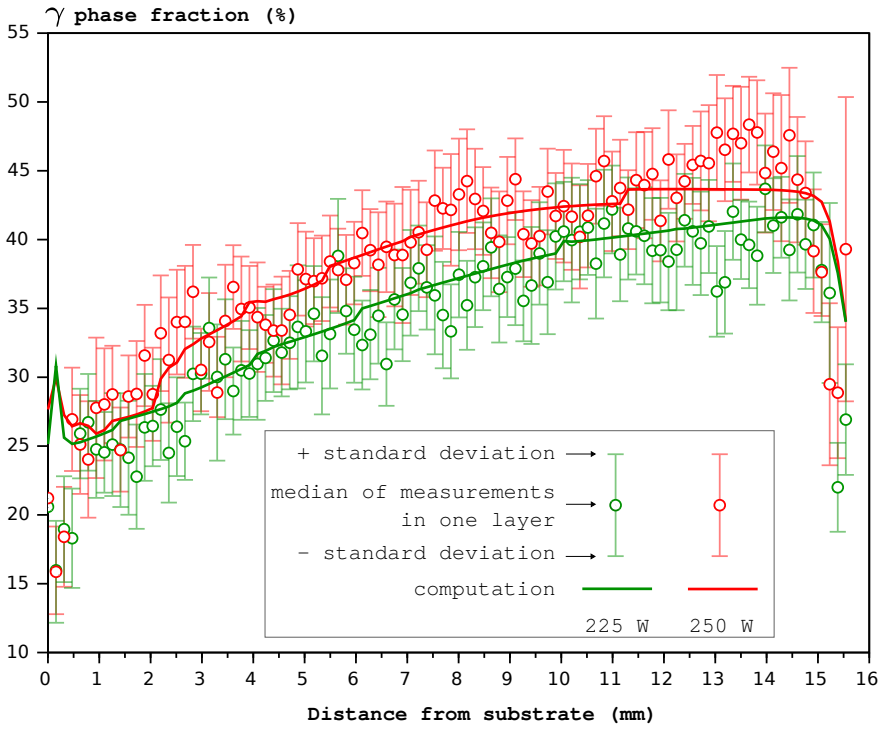

Figure 12: Comparison of measured and computed γ phase fraction for 225 and 250 W.

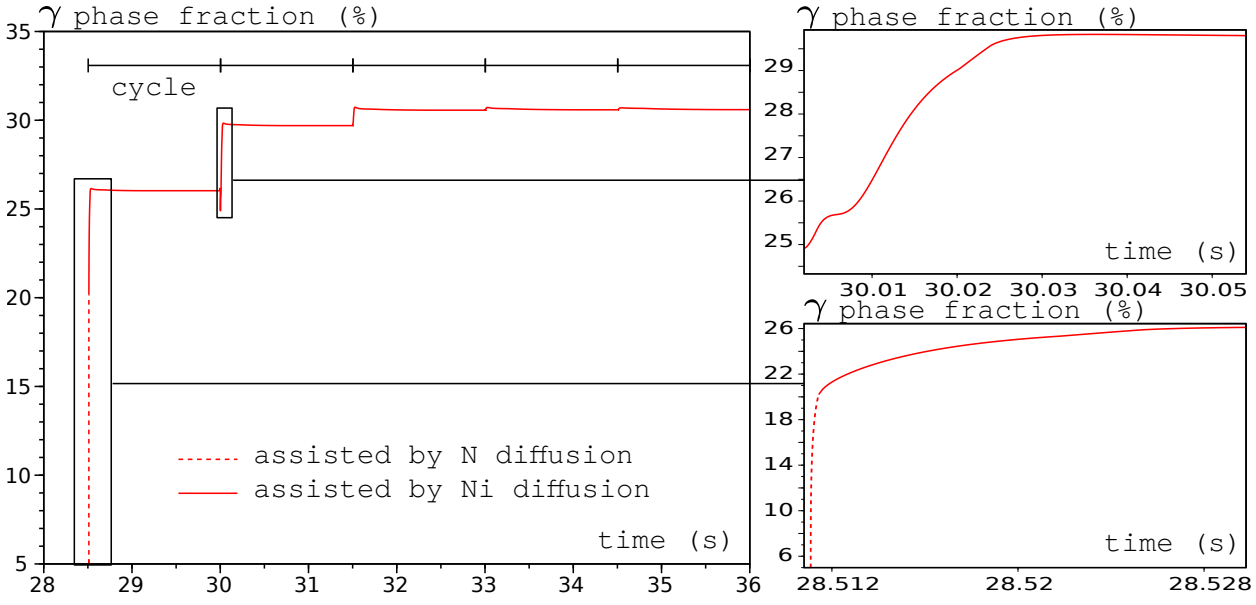

Figure 13: Influence of thermal cycling on phase transition (20-th layer, 250 W).

distribution in the part and ferrite to austenite phase ratios closer to 50/50, one can imagine to control the substrate temperature during fabrication using heating/cooling device with a control

loop. The proposed temperature profile linearly decreases from 1000 K for the first layer to 800 K for the last layer. Results are presented in figure 14 and compared to the reference computation without temperature control of the substrate. This example shows almost uniform phase fraction distribution may be obtained with a ferrite to austenite phase ratio close to the targeted 50/50.

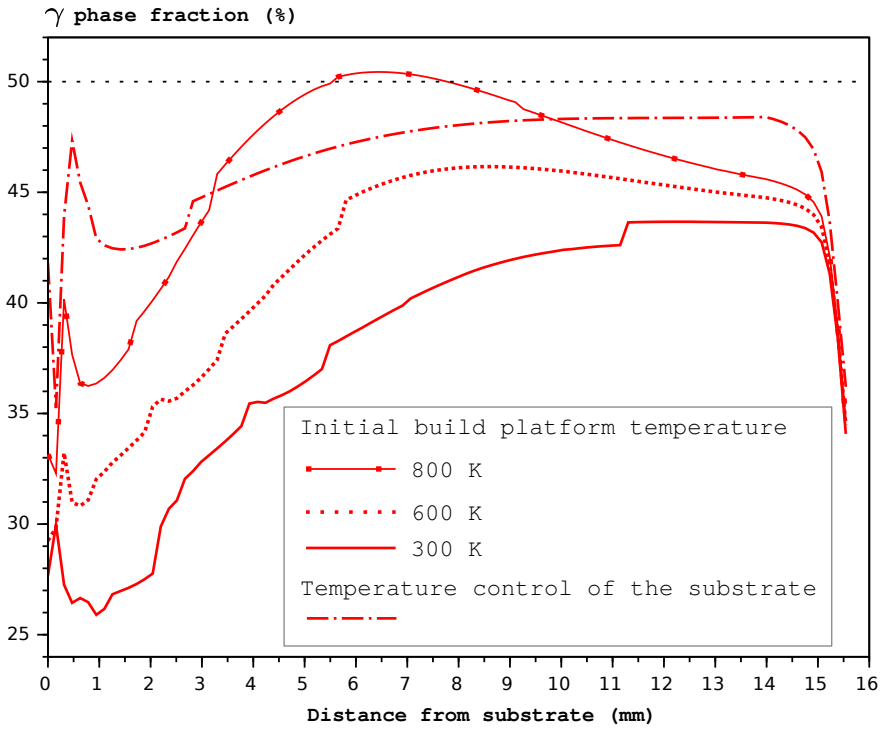

Figure 14: γ phase fraction for different initial build platform temperatures and for controlled temperature of the build platform.

Of course this simple analysis does not replace a proper parametric study for each specific part. Indeed there is a complex interweaving between process parameters such as laser power and speed, scanning strategy, dwell time, build platform temperature control etc., and properties of the build such as the deposition temperature (see. equation (1)), layer height and thickness (as reported for instance in [53]), grain size, all having a significant influence on the phase transition kinetics. However, the tools proposed in this contribution enables to reach sufficiently short computation time to be able to optimize the phase fraction ratio in DSS parts.

7. Conclusion

In this paper an experimental study enabled to characterise the microstructure (grain morphology and austenite to ferrite ratio) in a super duplex stainless steel (i.e., SAF-2507) obtained by directed energy deposition additive manufacturing. The thermal history in this fabrication process being rather complex, heterogeneous phase fraction distributions have been observed, and higher power is associated with higher austenite phase fraction. After around 50 layers phase fraction

profiles tend to stabilize to a ferrite to austenite phase ratio near 55/45 for 250 W and 60/40 for 225 W.

Since such duplex stainless steel alloys necessitate ferrite to austenite phase ratio near 50/50 in the entire part, a fast numerical approach (temperature and diffusion controlled phase transition) has been developed to optimize process parameters in order to reach a more uniform phase fraction distribution. Numerical results have been compared to the experiments and a reasonable agreement has been observed. In addition, the model has then been tested to determine suitable temperature control of the build platform in order to reach the desired phase fraction distribution. In addition, the proposed simulation tool is sufficiently fast to consider parametric studies or optimization loops in order to facilitate additive manufacturing of super duplex stainless steels and other alloys undergoing diffusion controlled solid state phase transitions.

Acknowledgement

This work received funding from the QUADS project of the Agence Innovation Défense (Ministry of army).

Appendix A. Analytical solution of the substrate temperature

In this section the 1D heat conduction problem (2) with boundary conditions (3) and initial condition (4) is solved analytically. Separation of variables enables to write the solution in the form:

$$T^n_{\text{sub}}(Z,t) = \sum_{j=1}^{N} \left(T^n_j \cos\left(\frac{Z}{Z_j}\right) + \tilde{T}^n_j \sin\left(\frac{Z}{Z_j}\right) \right) \exp\left(-\frac{D_{\text{sub}}}{Z_j^2} t\right) + T^n_1 \frac{Z}{h_{\text{sub}}} + T^n_0 \tag{A.1}$$

where T^n_j, T^n_1, T^n_0 are unknown coefficients to be determined. The boundary conditions (3) combined with (A.1) lead to:

$$\begin{pmatrix} T^n_1 \\ T^n_0 \end{pmatrix} = - \begin{pmatrix} -\left(\frac{\lambda_{\text{sub}}}{h_{\text{sub}}} + \frac{H_{\text{build}}}{2}\right) & -H_{\text{build}} \\ \left(\frac{\lambda_{\text{sub}}}{h_{\text{sub}}} + \frac{H_{\text{plate}}}{2}\right) & -H_{\text{plate}} \end{pmatrix}^{-1} \cdot \begin{pmatrix} H_{\text{build}}\, T^n_{\text{build}} \\ H_{\text{plate}}\, T_{\text{plate}} \end{pmatrix} \tag{A.2}$$

and for all $1 \leq j \leq N$:

$$\begin{pmatrix} A^+_j & -B^+_j \\ A^-_j & B^-_j \end{pmatrix} \cdot \begin{pmatrix} T^n_j \\ \tilde{T}^n_j \end{pmatrix} = \cdot \begin{pmatrix} 0 \\ 0 \end{pmatrix} \tag{A.3}$$

where:

$$\begin{cases} A^+_j = \dfrac{\lambda_{\text{sub}}}{Z_j} \sin\left(\dfrac{h_{\text{sub}}}{2Z_j}\right) - H_{\text{build}} \cos\left(\dfrac{h_{\text{sub}}}{2Z_j}\right) \\ A^-_j = \dfrac{\lambda_{\text{sub}}}{Z_j} \sin\left(\dfrac{h_{\text{sub}}}{2Z_j}\right) - H_{\text{plate}} \cos\left(\dfrac{h_{\text{sub}}}{2Z_j}\right) \\ B^+_j = \dfrac{\lambda_{\text{sub}}}{Z_j} \cos\left(\dfrac{h_{\text{sub}}}{2Z_j}\right) + H_{\text{build}} \sin\left(\dfrac{h_{\text{sub}}}{2Z_j}\right) \\ B^-_j = \dfrac{\lambda_{\text{sub}}}{Z_j} \cos\left(\dfrac{h_{\text{sub}}}{2Z_j}\right) + H_{\text{plate}} \sin\left(\dfrac{h_{\text{sub}}}{2Z_j}\right) \end{cases} \tag{A.4}$$

Therefore, Z_j are defined as successive positive roots of $A_j^+ B_j^- + A_j^- B_j^+ = 0$, and the following relation holds: $\widetilde{T}_j^n = (A_j^+/B_j^+)T_j^n$. Thus the last coefficients to determine are T_j^n. The initial condition (4) involves the substrate temperature at the end of the previous layer deposition, which reads:

$$T_{\text{sub}}^{n-1}(Z, t^{n-1}) = \sum_{j=1}^{N} T_j^{n-1} f_j\left(\frac{Z}{Z_j}\right) \exp\left(-\frac{D_{\text{sub}}}{Z_j^2} t^{n-1}\right) + T_1^{n-1}\frac{Z}{h_{\text{sub}}} + T_0^{n-1} \tag{A.5}$$

where we defined the eigenfunctions:

$$f_j : y \mapsto \left(\cos(y) + \frac{A_j^+}{B_j^+}\sin(y)\right) \tag{A.6}$$

Because of orthogonality of the eigenfunctions f_j with respect to the inner product (A.8) one obtains:

$$T_j = T_j^{n-1}\exp\left(-\frac{D_{\text{sub}}}{Z_j^2} t^{n-1}\right) + \frac{T_1^{n-1} - T_1^n}{h_{\text{sub}}}\frac{\langle Z, f_j\rangle}{\langle f_j, f_j\rangle} + (T_0^{n-1} - T_0^n)\frac{\langle 1, f_j\rangle}{\langle f_j, f_j\rangle} \tag{A.7}$$

where the usual inner product has been defined:

$$\langle f, g\rangle = \int_{-\frac{h_{\text{sub}}}{2}}^{\frac{h_{\text{sub}}}{2}} f(Z)\, g(Z)\mathrm{d}Z \tag{A.8}$$

Appendix B. Analytical solution of the diffusion problem

In this section the analytical solution of (5) subjected to boundary conditions (6) and initial condition (7) is derived for slabs, cylinders and sphere (i.e., for $q = 0, 1, 2$). The equation is solved by separation of variables and the solution reads:

$$\begin{cases} c_k^\delta(x,t) = \displaystyle\sum_{j=1}^{N} c_{j,k}^\delta\, f\left(\frac{x}{x_{j,k}^\delta}\right) \exp\left(-\frac{D_k^\delta}{\left(x_{j,k}^\delta\right)^2}(t - t_k)\right) + c_{\text{eq},k}^\delta & \text{if} \quad 0 \le x \le R - w_k \\ c_k^\gamma(x,t) = \displaystyle\sum_{j=1}^{N} \left(c_{j,k}^\gamma\, f\left(\frac{x}{x_{j,k}^\gamma}\right) + \widetilde{c}_{j,k}^\gamma\, g\left(\frac{x}{x_{j,k}^\gamma}\right)\right) \exp\left(-\frac{D_k^\gamma}{\left(x_{j,k}^\gamma\right)^2}(t - t_k)\right) + c_{\text{eq},k}^\gamma & \text{if} \quad R - w_k \le x \le R \end{cases} \tag{B.1}$$

where $c_{j,k}^\delta, c_{j,k}^\gamma, \widetilde{c}_{j,k}^\gamma$ are unknown coefficients, $x_{j,k}^\delta, x_{j,k}^\gamma$ are the eigenvalues to be determined, and f and g are the following eigenfunctions:

	$q = 0$	$q = 1$	$q = 2$
$f(x)$	$\cos(x)$	$J_0(x)$	$\dfrac{\sin(x)}{x}$
$g(x)$	$\sin(x)$	$Y_0(x)$	$\dfrac{\cos(x)}{x}$

(B.2)

where J_p and Y_p denote the p-th order Bessel functions of the first and second kind respectively. Eigenvalues $x^{\delta}_{j,k}, x^{\gamma}_{j,k}$ are determined by using boundary conditions (6), which lead to:

$$f\left(\frac{R-w_k}{x^{\delta}_{j,k}}\right)=0 \quad \text{and} \quad \begin{pmatrix} f\left(\frac{R-w_k}{x^{\gamma}_{j,k}}\right) & g\left(\frac{R-w_k}{x^{\gamma}_{j,k}}\right) \\ f'\left(\frac{R}{x^{\gamma}_{j,k}}\right) & g'\left(\frac{R}{x^{\gamma}_{j,k}}\right) \end{pmatrix} \cdot \begin{pmatrix} c^{\gamma}_{j,k} \\ \widetilde{c}^{\gamma}_{j,k} \end{pmatrix} = \begin{pmatrix} 0 \\ 0 \end{pmatrix} \tag{B.3}$$

hence non trivial solution are obtained by computing the roots of the matrix determinant in (B.3):

$$f\left(\frac{R-w_k}{x^{\gamma}_{j,k}}\right) g'\left(\frac{R}{x^{\gamma}_{j,k}}\right) - f'\left(\frac{R}{x^{\gamma}_{j,k}}\right) g\left(\frac{R-w_k}{x^{\gamma}_{j,k}}\right) = 0 \tag{B.4}$$

and:

$$\widetilde{c}^{\gamma}_{j,k} = -\frac{f\left(\frac{R-w_k}{x^{\gamma}_{j,k}}\right)}{g\left(\frac{R-w_k}{x^{\gamma}_{j,k}}\right)} c^{\gamma}_{j,k} \tag{B.5}$$

Therefore the eigenvalues read:

	$q=0$	$q=1$	$q=2$
$x^{\delta}_{j,k}$	$\frac{R-w_k}{\frac{\pi}{2}+j\,\pi}$	$\frac{R-w_k}{\zeta_j}$	$\frac{R-w_k}{j\,\pi}$
$x^{\gamma}_{j,k}$	$\frac{w_k}{\frac{\pi}{2}+j\,\pi}$	$\frac{w_k}{\xi_j}$	$\frac{w_k}{\chi_{j,k}}$

(B.6)

where ζ_j ($1 \leq j \leq N$) are the positive successive zero of the 0-order Bessel function of the first kind J_0, which are known, $\chi_{j,k}$ are the positive successive roots of $\chi \mapsto (\chi - (w_k/R)\tan(\chi))$, and $\xi_{j,k}$ are the positive successive roots of $\xi \mapsto T_1(R/w_k\,\xi) - T_0((R/w_k - 1)\,\xi)$ (where $T_p = J_p/Y_p$). Therefore, it is clear from (B.6) that the eigenvalues $x^{\delta}_{j,k}$ are fairly easy to compute for each time step k as explicit formulae have been obtained. However, for $q = 1, 2$ the eigenvalues $x^{\gamma}_{j,k}$ necessitate to numerically solve non-linear equations that depend on the time step k. Thus, the computation cost is much higher if there is a large number of time steps. Fortunately for slabs (i.e., $q = 0$) the eigenvalues $x^{\gamma}_{j,k}$ are also given explicitly, which enables to reach very short computation times.

Unknown coefficients $c^{\delta}_{j,k}, c^{\gamma}_{j,k}, \widetilde{c}^{\gamma}_{j,k}$ are determined by applying the initial condition (7). Considering the following orthogonality relations:

$$\begin{cases} \left\langle f\left(x/x^{\delta}_{i,k}\right), f\left(x/x^{\delta}_{j,k}\right)\right\rangle^{\delta}_{k} = \begin{cases} 0 & \text{if} \quad i \neq j \\ \neq 0 & \text{if} \quad i = j \end{cases} \\ \left\langle f\left(x/x^{\gamma}_{i,k}\right), f\left(x/x^{\gamma}_{j,k}\right)\right\rangle^{\gamma}_{k} = \begin{cases} 0 & \text{if} \quad i \neq j \\ \neq 0 & \text{if} \quad i = j \end{cases} \\ \left\langle g\left(x/x^{\gamma}_{i,k}\right), g\left(x/x^{\gamma}_{j,k}\right)\right\rangle^{\gamma}_{k} = \begin{cases} 0 & \text{if} \quad i \neq j \\ \neq 0 & \text{if} \quad i = j \end{cases} \\ \left\langle f\left(x/x^{\gamma}_{i,k}\right), g\left(x/x^{\gamma}_{j,k}\right)\right\rangle^{\gamma}_{k} = 0 \end{cases} \tag{B.7}$$

where the inner products are defined as follows:

$$\begin{cases} \langle f_1, f_2 \rangle_k^{\delta} = \displaystyle\int_0^{R-w_k} x^q f_1(x) f_2(x) \mathrm{d}x \\ \langle f_1, f_2 \rangle_k^{\gamma} = \displaystyle\int_{R-w_k}^{R} x^q f_1(x) f_2(x) \mathrm{d}x \end{cases} \tag{B.8}$$

the coefficients read:

$$\begin{cases} c_{j,k}^{\delta} = \dfrac{\left\langle f(x/x_{j,k}^{\delta}), c_{\mathrm{ini},k}^{\delta}(x) \right\rangle_k^{\delta}}{\left\langle f(x/x_{j,k}^{\delta}), f(x/x_{j,k}^{\delta}) \right\rangle_k^{\delta}} \\ c_{j,k}^{\gamma} = \dfrac{\left\langle f(x/x_{j,k}^{\gamma}), c_{\mathrm{ini},k}^{\gamma}(x) \right\rangle_k^{\gamma}}{\left\langle f(x/x_{j,k}^{\gamma}), f(x/x_{j,k}^{\gamma}) \right\rangle_k^{\gamma}} \\ \widetilde{c}_{j,k}^{\gamma} = \dfrac{\left\langle g(x/x_{j,k}^{\gamma}), c_{\mathrm{ini},k}^{\gamma}(x) \right\rangle_k^{\gamma}}{\left\langle g(x/x_{j,k}^{\gamma}), g(x/x_{j,k}^{\gamma}) \right\rangle_k^{\gamma}} \end{cases} \tag{B.9}$$

Using (8) along with (B.1) it is clear that $c_{\mathrm{ini},k}^{\delta}, c_{\mathrm{ini},k}^{\gamma}$ are given analytically and involves the same eigenfunctions f and g, which enables to compute analytically the inner products in (B.9).

The update of the austenite thickness given in (11) reads:

$$\begin{aligned} w_k = w_{k-1} &+ D_{k-1}^{\delta} \sum_{j=1}^{N} c_{j,k}^{\delta} f'\left(\frac{x}{x_{j,k}^{\delta}}\right)\left(\frac{x_{j,k}^{\delta}}{D_k^{\delta}}\right)\left(1-\exp\left(-\frac{D_k^{\delta}}{\left(x_{j,k}^{\delta}\right)^2}\Delta t_k\right)\right) \\ &- D_{k-1}^{\gamma} \sum_{j=1}^{N} c_{j,k}^{\gamma}\left(f'\left(\frac{x}{x_{j,k}^{\gamma}}\right) - \frac{f\left(\frac{R-w_k}{x_{j,k}^{\gamma}}\right)}{g\left(\frac{R-w_k}{x_{j,k}^{\gamma}}\right)} g'\left(\frac{x}{x_{j,k}^{\gamma}}\right)\right)\left(\frac{x_{j,k}^{\gamma}}{D_k^{\gamma}}\right)\left(1-\exp\left(-\frac{D_k^{\gamma}}{\left(x_{j,k}^{\gamma}\right)^2}\Delta t_k\right)\right) \end{aligned} \tag{B.10}$$

References

[1] J.-S. Lim, W.-J. Oh, C.-M. Lee, D.-H. Kim, Selection of effective manufacturing conditions for directed energy deposition process using machine learning methods, Scientific reports 11 (2021) 1–13.

[2] P. Bajaj, A. Hariharan, A. Kini, P. Kürnsteiner, D. Raabe, E. Jägle, Steels in additive manufacturing: A review of their microstructure and properties, Materials Science and Engineering: A 772 (2020) 138633.

[3] J.-O. Nilsson, Super duplex stainless steels, Materials science and technology 8 (1992) 685–700.

[4] M. Knyazeva, M. Pohl, Duplex steels: Part i: Genesis, formation, structure, Metallography, Microstructure, and Analysis 2 (2013) 113–121.

[5] I. Calliari, M. Pellizzari, M. Zanellato, E. Ramous, The phase stability in cr–ni and cr–mn duplex stainless steels, Journal of materials science 46 (2011) 6916–6924.

[6] A. Ramirez, J. Lippold, S. Brandi, The relationship between chromium nitride and secondary austenite precipitation in duplex stainless steels, Metallurgical and materials transactions A 34 (2003) 1575–1597.

[7] S. Hertzman, B. Brolund, P. J. Ferreira, An experimental and theoretical study of heat-affected zone austenite reformation in three duplex stainless steels, Metallurgical and materials transactions A 28 (1997) 277–285.

[8] N. Pettersson, S. Wessman, S. Hertzman, A. Studer, High-temperature phase equilibria of duplex stainless steels assessed with a novel in-situ neutron scattering approach, Metallurgical and Materials Transactions A 48 (2017) 1562–1571.
[9] J.-O. Andersson, T. Helander, L. Höglund, P. Shi, B. Sundman, Thermo-calc & dictra, computational tools for materials science, Calphad 26 (2002) 273–312.
[10] F. Hengsbach, P. Koppa, K. Duschik, M. J. Holzweissig, M. Burns, J. Nellesen, W. Tillmann, T. Tröster, K.-P. Hoyer, M. Schaper, Duplex stainless steel fabricated by selective laser melting - Microstructural and mechanical properties, Materials & Design 133 (2017) 136–142.
[11] J. Kunz, A. Boontanom, S. Herzog, P. Suwanpinij, A. Kaletsch, C. Broeckmann, Influence of hot isostatic pressing post-treatment on the microstructure and mechanical behavior of standard and super duplex stainless steel produced by laser powder bed fusion, Materials Science and Engineering: A 794 (2020) 139806.
[12] D. Zhang, A. Liu, B. Yin, P. Wen, Additive manufacturing of duplex stainless steels-a critical review, Journal of Manufacturing Processes 73 (2022) 496–517.
[13] M. Eriksson, M. Lervåg, C. Sørensen, A. Robertstad, B. M. Brønstad, B. Nyhus, R. Aune, X. Ren, O. M. Akselsen, Additive manufacture of superduplex stainless steel using WAAM, MATEC Web of Conferences 188 (2018) 03014.
[14] K. Saeidi, L. Kevetkova, F. Lofaj, Z. Shen, Novel ferritic stainless steel formed by laser melting from duplex stainless steel powder with advanced mechanical properties and high ductility, Materials Science and Engineering: A 665 (2016) 59–65.
[15] A. R. Kannan, N. S. Shanmugam, V. Rajkumar, M. Vishnukumar, Insight into the microstructural features and corrosion properties of wire arc additive manufactured super duplex stainless steel (er2594), Materials Letters 270 (2020) 127680.
[16] M. Brázda, P. Salvetr, J. Dlouhỳ, J. Vavřík, Influence of laser power in direct laser deposition on the proportion of ferrite and austenite in duplex steel saf2507, in: METAL 2020-29th International Conference on Metallurgy and Materials, Conference Proceedings, pp. 539–544.
[17] A. D. Iams, J. S. Keist, T. A. Palmer, Formation of Austenite in Additively Manufactured and Post-Processed Duplex Stainless Steel Alloys, Metallurgical and Materials Transactions A 51 (2020) 982–999.
[18] Y. Lian, S. Lin, W. Yan, W. K. Liu, G. J. Wagner, A parallelized three-dimensional cellular automaton model for grain growth during additive manufacturing, Computational Mechanics 61 (2018) 543–558.
[19] H. Wei, G. Knapp, T. Mukherjee, T. DebRoy, Three-dimensional grain growth during multi-layer printing of a nickel-based alloy inconel 718, Additive Manufacturing 25 (2019) 448–459.
[20] C. Kumara, A. Segerstark, F. Hanning, N. Dixit, S. Joshi, J. Moverare, P. Nylén, Microstructure modelling of laser metal powder directed energy deposition of alloy 718, Additive Manufacturing 25 (2019) 357–364.
[21] J. Smith, W. Xiong, J. Cao, W. K. Liu, Thermodynamically consistent microstructure prediction of additively manufactured materials, Computational mechanics 57 (2016) 359–370.
[22] D. Zhang, Z. Feng, C. Wang, Z. Liu, D. Dong, Y. Zhou, R. Wu, Modeling of temperature field evolution during multilayered direct laser metal deposition, Journal of Thermal Spray Technology 26 (2017) 831–845.
[23] C. Baykasoglu, O. Akyildiz, D. Candemir, Q. Yang, A. C. To, Predicting microstructure evolution during directed energy deposition additive manufacturing of ti-6al-4v, Journal of Manufacturing Science and Engineering 140 (2018) 051003.
[24] J. Li, Q. Wang, P. P. Michaleris, An analytical computation of temperature field evolved in directed energy deposition, Journal of Manufacturing Science and Engineering 140 (2018) 101004.
[25] C. Guévenoux, M. Nasiry, S. Durbecq, A. Charles, E. Charkaluk, A. Constantinescu, Thermal modeling of ded repair process for slender panels by a 2d semi-analytic approach (2020).
[26] D. Weisz-Patrault, Fast simulation of temperature and phase transitions in directed energy deposition additive manufacturing, Additive Manufacturing 31 (2020) 100990.
[27] D. Weisz-Patrault, Fast macroscopic thermal analysis for laser metal deposition. Application to multiphase steels, in: Sim-AM 2019: II International Conference on Simulation for Additive Manufacturing, CIMNE, pp. 60–71.
[28] D. Weisz-Patrault, P. Margerit, A. Constantinescu, Residual stresses in thin walled-structures manufactured by directed energy deposition: In-situ measurements, fast thermo-mechanical simulation and buckling, Additive Manufacturing (2022) 102903.

[29] D. Weisz-Patrault, S. Sakout, A. Ehrlacher, Fast simulation of temperature and grain growth in directed energy depostion additive manufacturing, in: 14th World Congress on Computational Mechanics, volume 1, ECCOMAS Congress, p. 2748.
[30] S. Sakout, D. Weisz-Patrault, A. Ehrlacher, Energetic upscaling strategy for grain growth. I: Fast mesoscopic model based on dissipation, Acta Materialia 196 (2020) 261–279.
[31] D. Weisz-Patrault, S. Sakout, A. Ehrlacher, Energetic upscaling strategy for grain growth. II: Probabilistic macroscopic model identified by Bayesian techniques, Acta Materialia (2021).
[32] A. Miodownik, N. Saunders, Modelling of materials properties in duplex stainless steels, Materials Science and Technology 18 (2002) 861–868.
[33] T. Berecz, É. Fazakas, I. Mészáros, I. Sajó, Decomposition kinetics of ferrite in isothermally aged saf 2507-type duplex stainless steel, Journal of Materials Engineering and Performance 24 (2015) 4777–4788.
[34] H. K. Bhadeshia, Diffusional formation of ferrite in iron and its alloys, Progress in Materials Science 29 (1985) 321–386.
[35] J. Vitek, S. Vitek, S. David, Numerical modeling of diffusion-controlled phase transformations in ternary systems and application to the ferrite/austenite transformation in the fe-cr-ni system, Metallurgical and Materials Transactions A 26 (1995) 2007–2025.
[36] J. Andersson, L. Höglund, B. Jönsson, J. Ågren, C. Purdy, Fundamentals and applications of ternary diffusion, New York (1990).
[37] S. Wessman, M. Selleby, Evaluation of austenite reformation in duplex stainless steel weld metal using computational thermodynamics, Welding in the World 58 (2014) 217–224.
[38] A. Jacob, E. Povoden-Karadeniz, Predictive computations of intermetallic σ phase evolution in duplex steel. i) thermodynamic modeling of σ phase in the fe–cr–mn–mo–ni system, Calphad 71 (2020) 101998.
[39] C. Herrera, N. De Lima, A. Kliauga, A. Padilha, Microstructure and texture of duplex stainless steel after melt-spinning processing, Materials Characterization 59 (2008) 79–83.
[40] D. Bäuerle, Laser processing and chemistry, Springer Science & Business Media, 2013.
[41] A. Prasad, L. Yuan, P. Lee, M. Patel, D. Qiu, M. Easton, D. StJohn, Towards understanding grain nucleation under additive manufacturing solidification conditions, Acta Materialia 195 (2020) 392–403.
[42] T. Quested, A. Greer, Grain refinement of al alloys: Mechanisms determining as-cast grain size in directional solidification, Acta Materialia 53 (2005) 4643–4653.
[43] J. D. Hunt, Steady state columnar and equiaxed growth of dendrites and eutectic, Materials science and engineering 65 (1984) 75–83.
[44] M. C. Flemings, Solidification processing, Metallurgical and Materials Transactions B 5 (1974) 2121–2134.
[45] J. Shao, G. Yu, X. He, S. Li, R. Chen, Y. Zhao, Grain size evolution under different cooling rate in laser additive manufacturing of superalloy, Optics & Laser Technology 119 (2019) 105662.
[46] N. Pryds, X. Huang, The effect of cooling rate on the microstructures formed during solidification of ferritic steel, Metallurgical and Materials Transactions A 31 (2000) 3155–3166.
[47] S. S. Ltd., Jmatpro, 2022.
[48] R. H. A. Abas, N. K. Taieh, Experimental study of the thermal diffusivity and heat capacity concerning some duplex stainless steel, Al-Khwarizmi Engineering Journal 11 (2015) 51–61.
[49] M. Bobadilla, A. Tschiptschin, On the nitrogen diffusion in a duplex stainless steel, Materials Research 18 (2015) 390–394.
[50] R. Zhou, D. O. Northwood, C. Liu, On nitrogen diffusion during solution treatment in a high nitrogen austenitic stainless steel, Journal of Materials Research and Technology 9 (2020) 2331–2337.
[51] B. Jönsson, Assessment of the mobilities of cr, fe and ni in bcc cr-fe-ni alloys, ISIJ international 35 (1995) 1415–1421.
[52] L. Kaufman, H. Bernstein, Computer calculation of phase diagrams. with special reference to refractory metals (1970).
[53] M. Bréhier, D. Weisz-Patrault, C. Tournier, Revisiting the influence of the scanning speed on surface topography and microstructure of in718 thin walls in directed energy deposition additive manufacturing, Procedia CIRP 108 (2022) 470–476.